Contents

1 Introduction

The measurements of field inetgrals and magnetic fields were carried out on October 28, 2015, after the cooling down of the undulator for the environmental tests.

The Beff repeatabilty measurements were carried out on October 29, 2015.

The 5 pointy off-axis measuremenst were carried out on November 10, 2015.

The 9 pointy off-axis measuremenst of the effective field were carried out on November 11, 2015.

2 Temperature cycle

The temperaturs during the temperature variation cycle were monitored by 6 temperature sensors. Figure 1 shows the location of the temperature sensors. Figure 2 shows the measured temperatures during the temperature variation cycle.

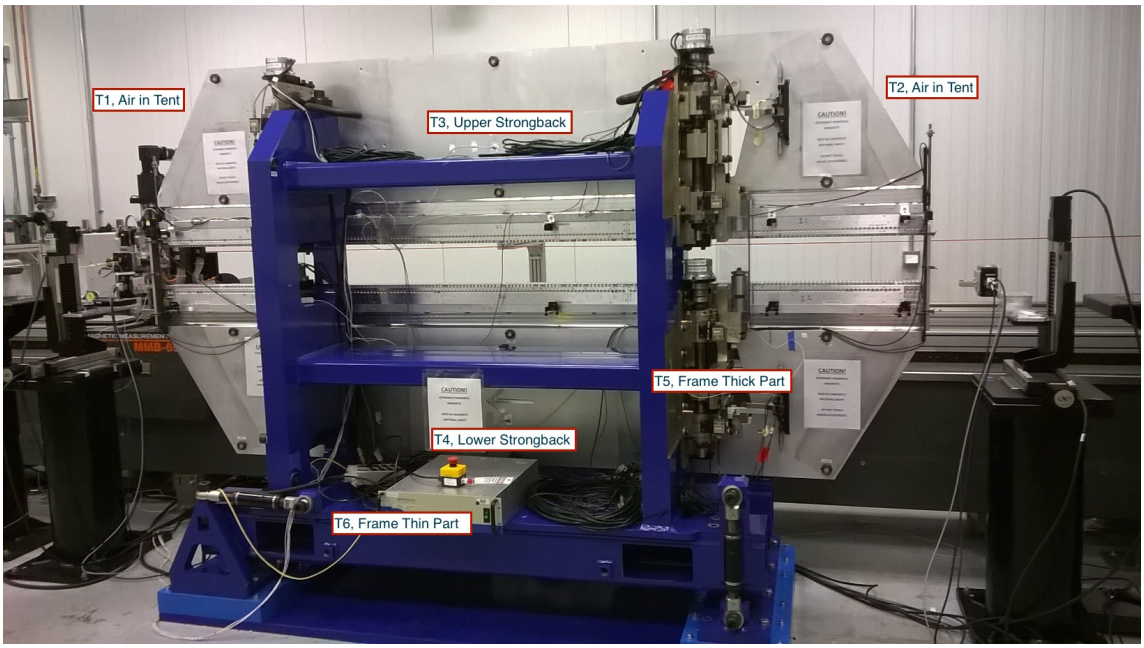

Figure 1: Location of the temperature sensors.

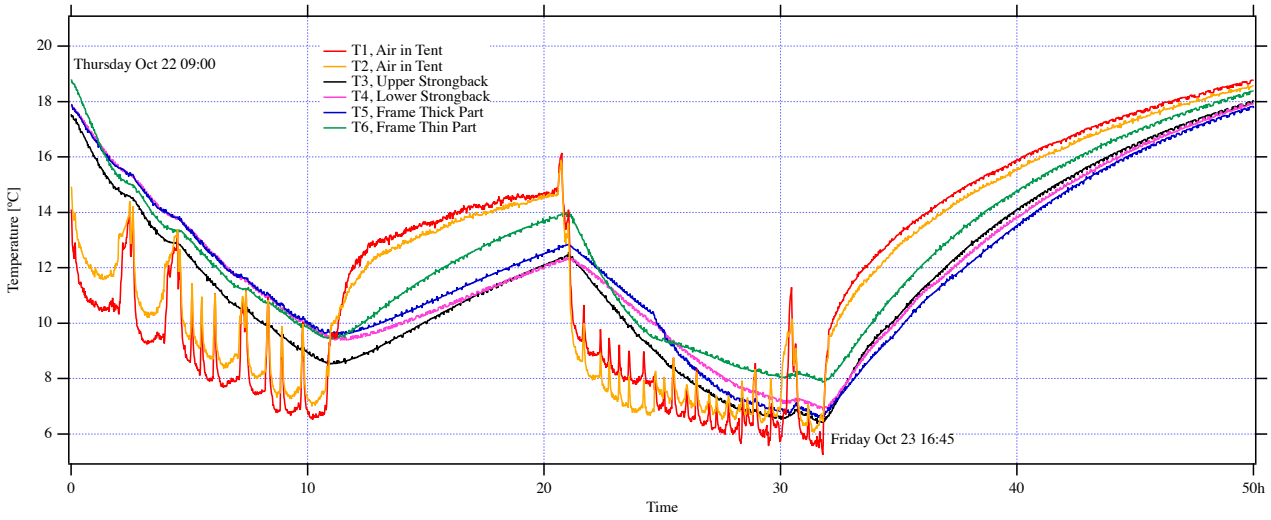

Figure 2: Measured temperature variation during the temperature cycle.

3 Center of undulator

The alignment fo the undulator relative to the Kugler bench was measured. The center is found by doing in total 10 Hall probe scans at different transverse positions around an estimated center line of the undulator.

In order to find the horizontal center, 5 Hall probe scans with a horizontal spaing of 2.5 mm were measured at the gap 25 mm. The horizontal position of the maxima of the peak field at each pole, which is fitted from the 5 points given by the scans, give the horizontal position of that pole. The horizontal position of all poles are used as shown in Figure 3 to find the horizontal center of the undulator at X = 84.95 mm in the coordinate system of the Kugler Hall probe bench.

In order to find the vertical center, 5 Hall probe scans with a vertical spaing of 0.5 mm were measured at the gap 10 mm. The vertical position of the minima of the peak field at each pole, which is fitted from the 5 points given by the scans, give the vertical center position at that pole. The vertical center position of all poles are used as shown in Figure 4 to find the vertical center of the undulator at -133.97 mm in the coordinate system of the Kugler Hall probe bench.

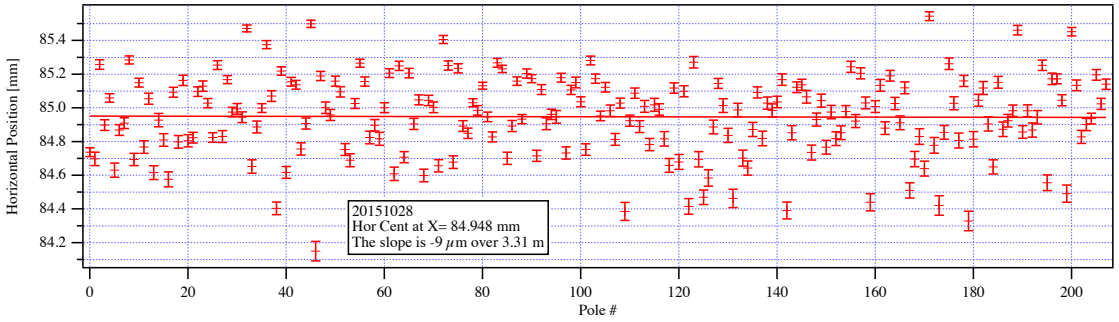

Figure 3: Horizontal center of the poles in the HXU-32.

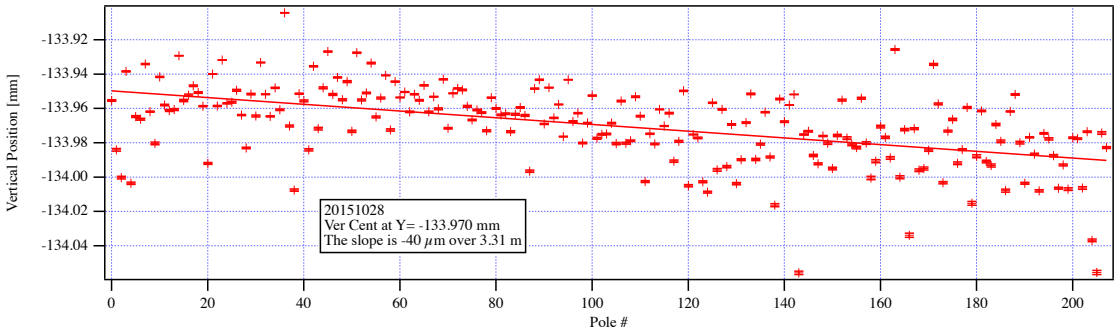

Figure 4: Vertical center of the poles in the HXU-32.

4 Field integrals

The field integrals are measured with a 3.735 m long flip coil. The diameter of the flip coil is approximately 4 mm. The vertical and horizontal field integrals have been measured on the vertical axis out from the horizontal center of the undulator in 2 mm steps out to ±20 mm horizontal deviation from the undulator axis. The multipoles up to octupole order have been found by fitting a cubic polynomial over the five central points over ±4 mm horizontal deviation from the undulator axis.

4.1 Vertical field integrals

Figure 5 shows the measured vertical field integrals at 9 different gaps. Table 1 gives the multipoles calculated from the measured field integrals by using a cubic polynomila over the 5 central points over the horizontal range ±4 mm out from the undulator axis. The background vertical field integral in UMF measured without an undulator installed is -125 Gcm.

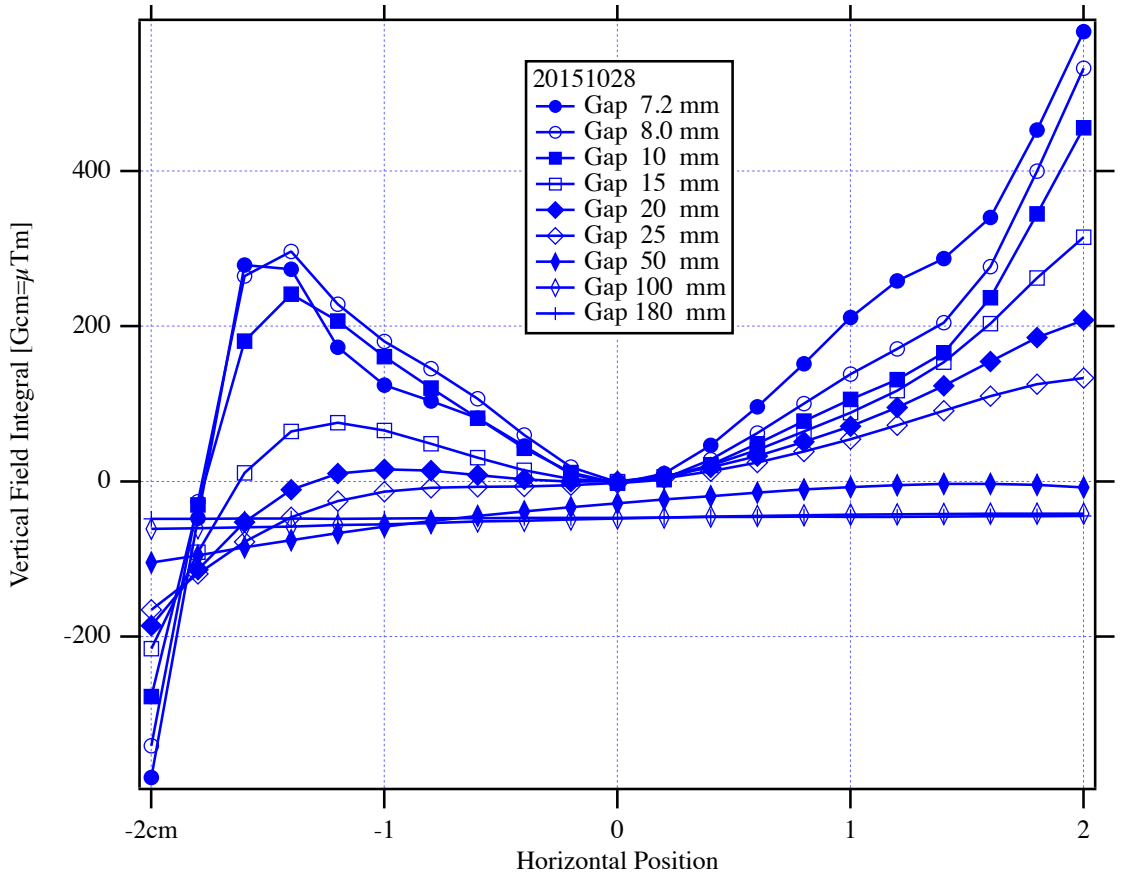

Figure 5: Vertical field integrals measured with a 3.735 m long flip coil.

4.2 Horizontal field integrals

Figure 6 shows the measured horizontal field integrals at 9 different gaps. Table 2 gives the skew multipoles calculated from the measured field integrals by using a cubic polynomila over the 5 central points over the horizontal range ±4 mm out from the undulator axis. The background horizontal field integral in UMF measured without an undulator installed is 47 Gcm.

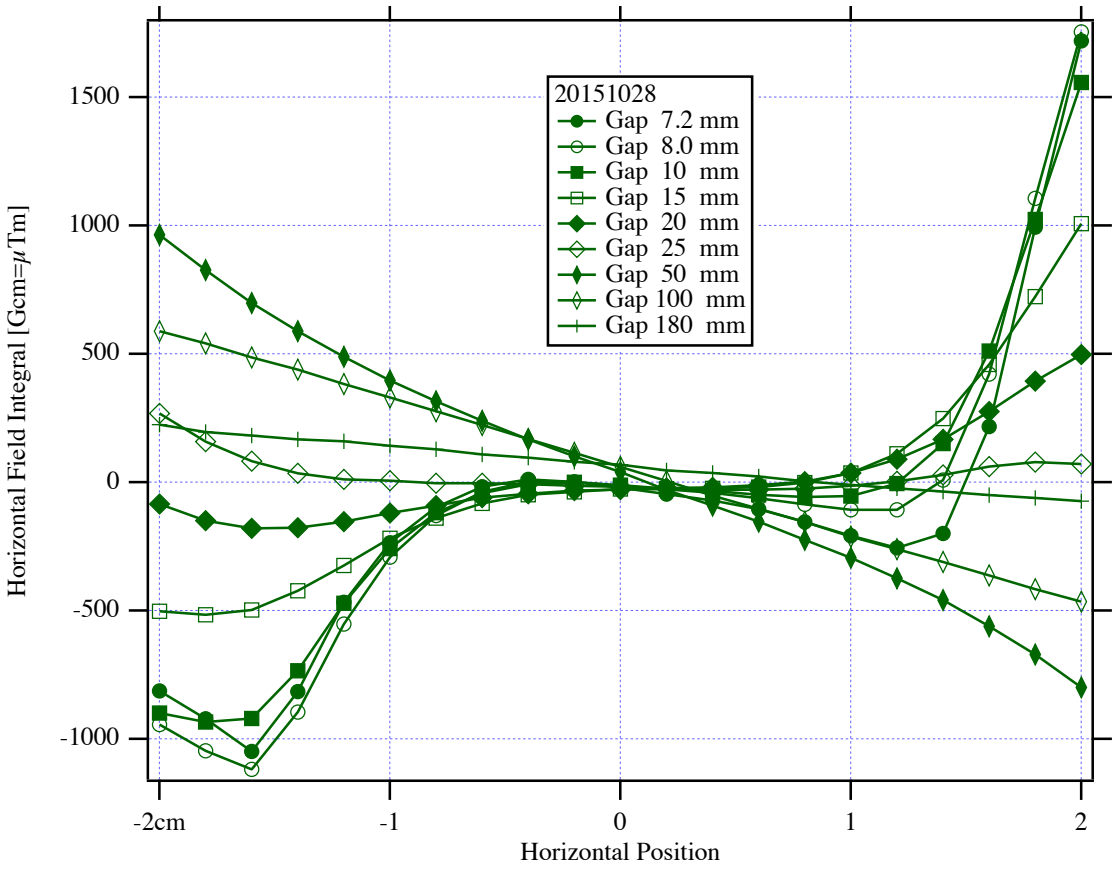

Figure 6: Horizontal field integrals measured with a 3.735 m long flip coil.

Table 1: Normal, i.e. vertical, multipoles.

Gap mm	Dipole Gcm	Quadrupole G	Sextupole G/cm	Octupole G/cm^2
7.2	-2 ±0.1	2 ±1	304 ±1.4	-2 ±6.9
8	-0 ±0.5	-37 ±3.2	278 ±4.5	-15 ±22.3
10	-2 ±0.3	-23 ±2.1	212 ±2.9	-22 ±14.3
15	0 ±0.3	8 ±1.9	109 ±2.7	-4 ±13.4
20	1 ±0.3	17 ±2.2	63 ±3.1	15 ±15.2
25	-2 ±0	21 ±0.2	32 ±0.3	22 ±1.7
50	-28 ±0.2	25 ±1.5	-4 ±2.1	-4 ±10.5
100	-47 ±0.1	6 ±0.4	-2 ±0.6	4 ±3.1
180	-47 ±0	1 ±0.3	2 ±0.5	2 ±2.2

Table 2: Skew, i.e. horizontal, multipoles.

Gap mm	Dipole Gcm	Quadrupole G	Sextupole G/cm	Octupole G/cm^2
7.2	-21 ±0.3	-123 ±1.8	-58 ±2.6	118 ±12.8
8	-12 ±1.4	-78 ±9.9	-46 ±13.9	151 ±68.3
10	-11 ±1.1	-70 ±7.5	-65 ±10.6	234 ±52.1
15	-29 ±2	25 ±13.5	-51 ±19	37 ±93.8
20	-27 ±1.4	20 ±9.2	-31 ±13	66 ±63.9
25	-18 ±1.1	-24 ±7.5	-4 ±10.6	-31 ±52.2
50	37 ±2.8	-328 ±18.8	4 ±26.5	27 ±130.5
100	60 ±0	-271 ±0.3	-16 ±0.5	-30 ±2.3
180	65 ±3.3	-83 ±22.5	3 ±31.6	47 ±156

5 Measured fields, angles, trajectories and phase errors

The magnetic fields have been measured on the undulator axis in 4400 mm long Hall probe scans. The field integral found with the flip coil is used for normalizing the magetic fields measured with the Hall probe system. The normalization is done by adding or subratcing a constant field over the magnetic structure of the undulator. The constant that is added corresponds to the difference between the flip coil and the Hall probe data over the length of the flip coil.

The Hall probe scans have been carried out at 9 different gaps; 7.2, 8.0, 10, 15, 20, 25, 50, 100, and 180 mm. The magnetic fields have been analyzed for the gap range 7.2-25 mm. In the analysis the function of the aoutocorrection system for the beam position in the accelerator has been simulated by using virtual coils in the beginning and end of the 4.4 m long scan to correct the orbit of the beam passing through the undulator.

5.1 Gap 7.2 mm

The measured fields, angles, trajectories and phase errors for the HXU-32 at 7.2 mm gap is shown in Figure 7 and Figure 8, which shows the same analysis with the beam path corrected by virtual coils in the beginning and end of the scan.

5.2 Gap 8.0 mm

The measured fields, angles, trajectories and phase errors for the HXU-32 at 8.0 mm gap is shown in Figure 9 and Figure 10, which shows the same analysis with the beam path corrected by virtual coils in the beginning and end of the scan.

5.3 Gap 10 mm

The measured fields, angles, trajectories and phase errors for the HXU-32 at 10 mm gap is shown in Figure 11 and Figure 12, which shows the same analysis with the beam path corrected by virtual coils in the beginning and end of the scan.

5.4 Gap 15 mm

The measured fields, angles, trajectories and phase errors for the HXU-32 at 15 mm gap is shown in Figure 13 and Figure 14, which shows the same analysis with the beam path corrected by virtual coils in the beginning and end of the scan.

5.5 Gap 20 mm

The measured fields, angles, trajectories and phase errors for the HXU-32 at 20 mm gap is shown in Figure 15 and Figure 16, which shows the same analysis with the beam path corrected by virtual coils in the beginning and end of the scan.

5.6 Gap 25 mm

The measured fields, angles, trajectories and phase errors for the HXU-32 at 25 mm gap is shown in Figure 17 and Figure 18, which shows the same analysis with the beam path corrected by virtual coils in the beginning and end of the scan.

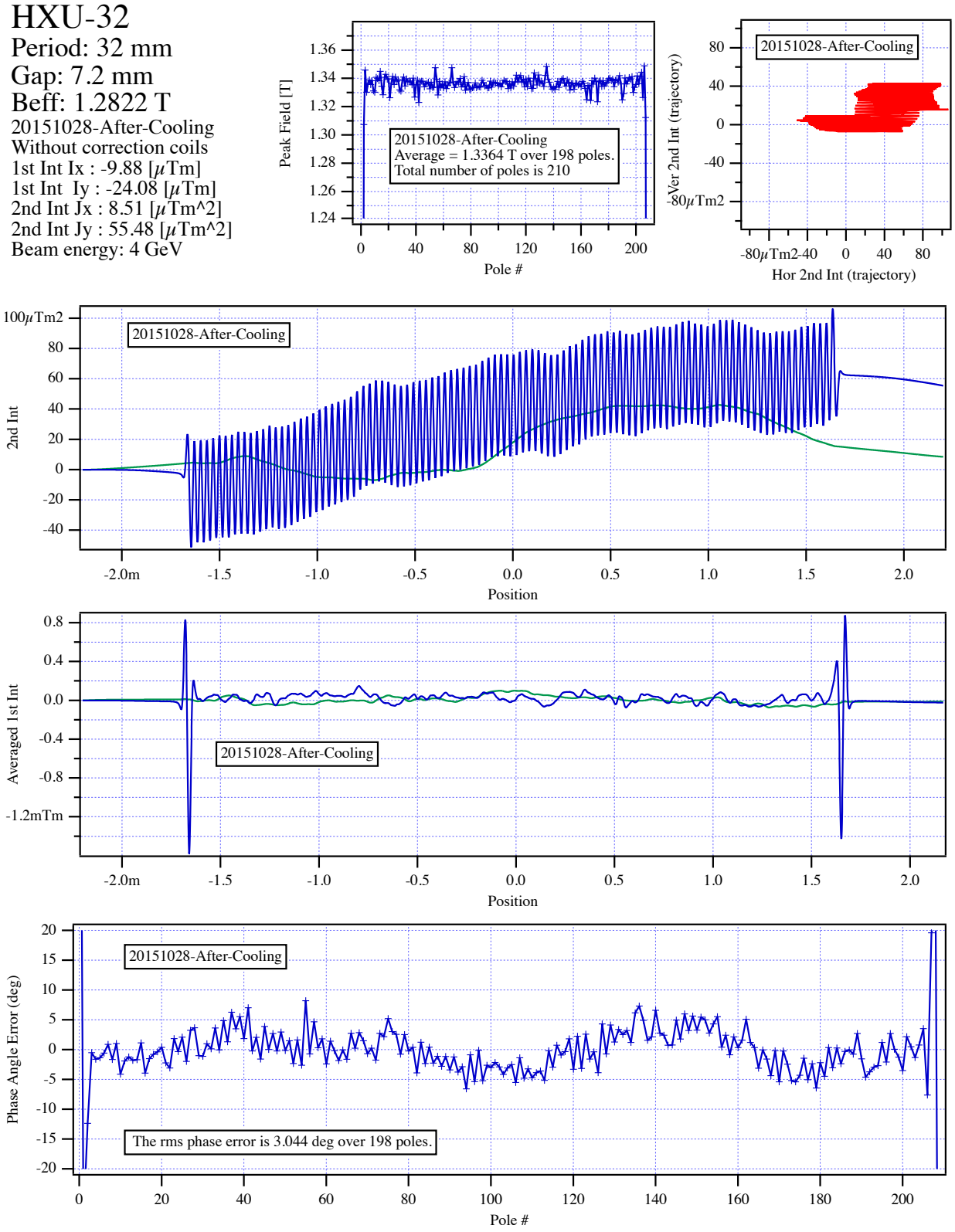

Figure 7: The measured fields, angles, trajectories and phase errors for the HXU-32 at 7.2 mm gap.

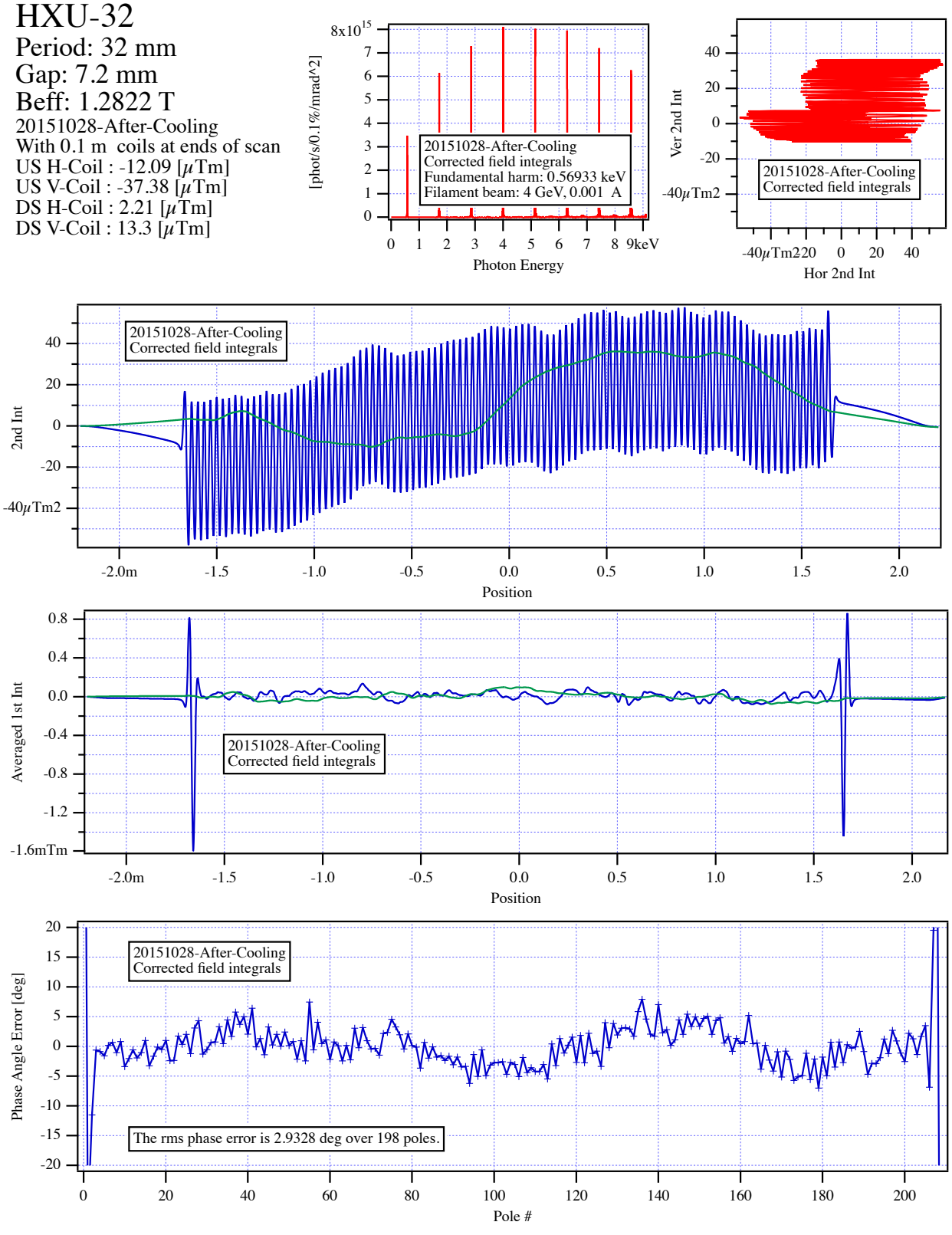

Figure 8: The measured fields, angles, trajectories and phase errors for the HXU-32 at 7.2 mm gap with the beam path corrected by virtual coils.

HXU-32
Period: 32 mm
Gap: 8 mm
Beff: 1.1587 T
20151028-After-Cooling
Without correction coils
1st Int Ix : -1.78 [μTm]
1st Int Iy : -22.28 [μTm]
2nd Int Jx : 35.62 [μTm^2]
2nd Int Jy : -24.69 [μTm^2]
Beam energy: 4 GeV

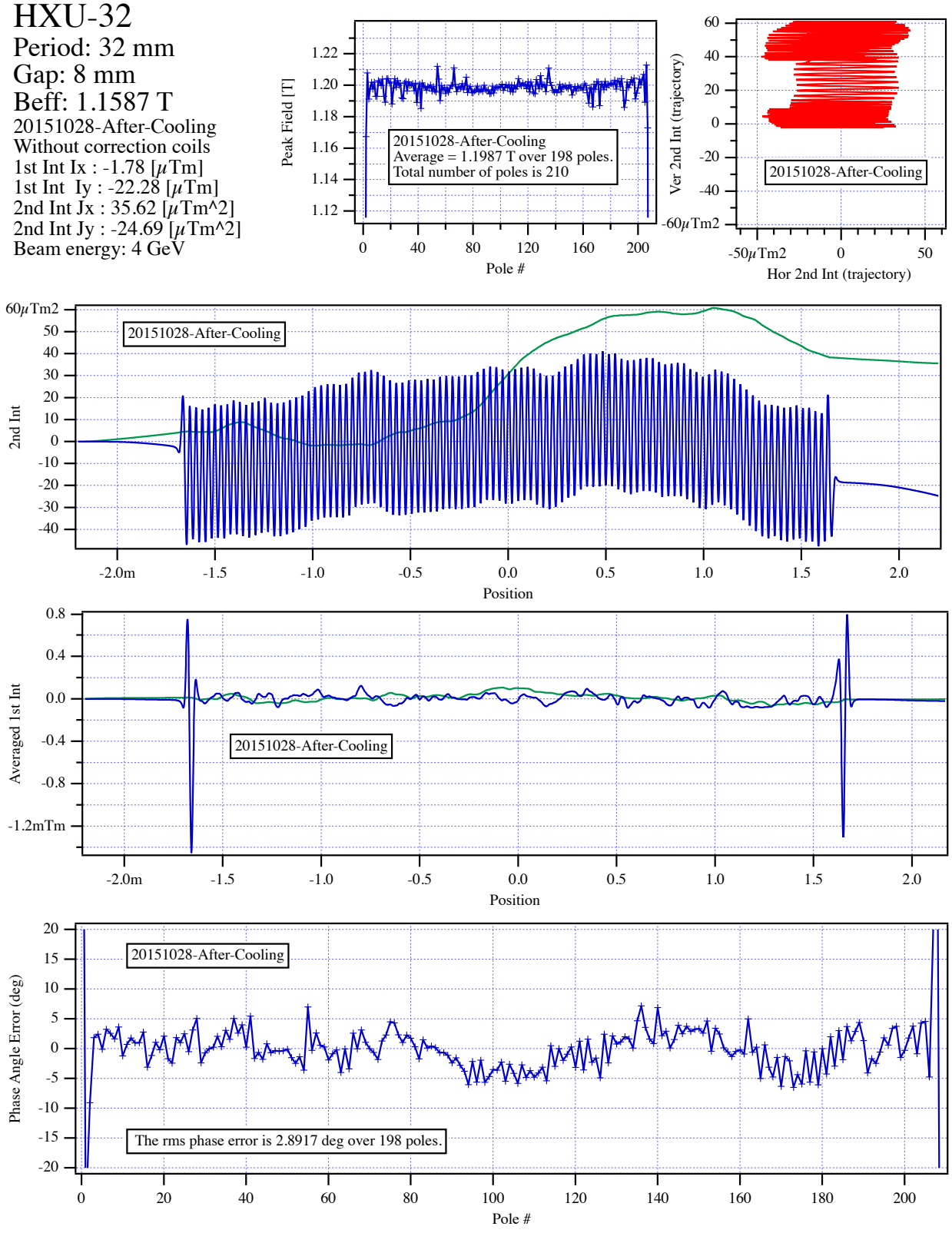

Figure 9: The measured fields, angles, trajectories and phase errors for the HXU-32 at 8.0 mm gap.

HXU-32
Period: 32 mm
Gap: 8 mm
Beff: 1.1587 T
20151028-After-Cooling
With 0.1 m coils at ends of scan
US H-Coil : -10.15 [μTm]
US V-Coil : -16.92 [μTm]
DS H-Coil : 8.38 [μTm]
DS V-Coil : -5.36 [μTm]

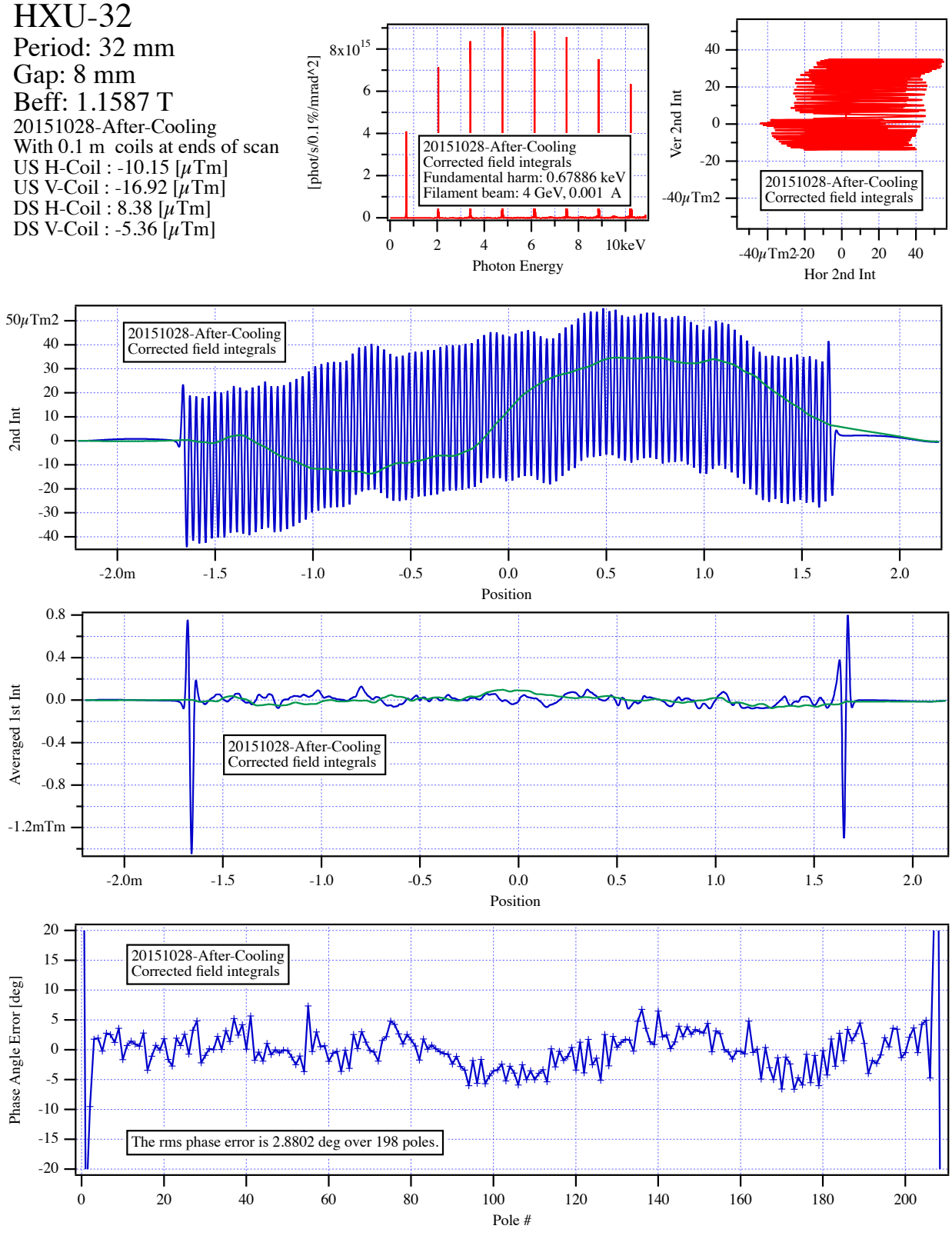

Figure 10: The measured fields, angles, trajectories and phase errors for the HXU-32 at 8.0 mm gap with the beam path corrected by virtual coils.

HXU-32
Period: 32 mm
Gap: 10 mm
Beff: 0.90493 T
20151028-After-Cooling
Without correction coils
1st Int Ix : -0.41 [μTm]
1st Int Iy : -23.27 [μTm]
2nd Int Jx : 35.84 [μTm^2]
2nd Int Jy : -22.44 [μTm^2]
Beam energy: 4 GeV

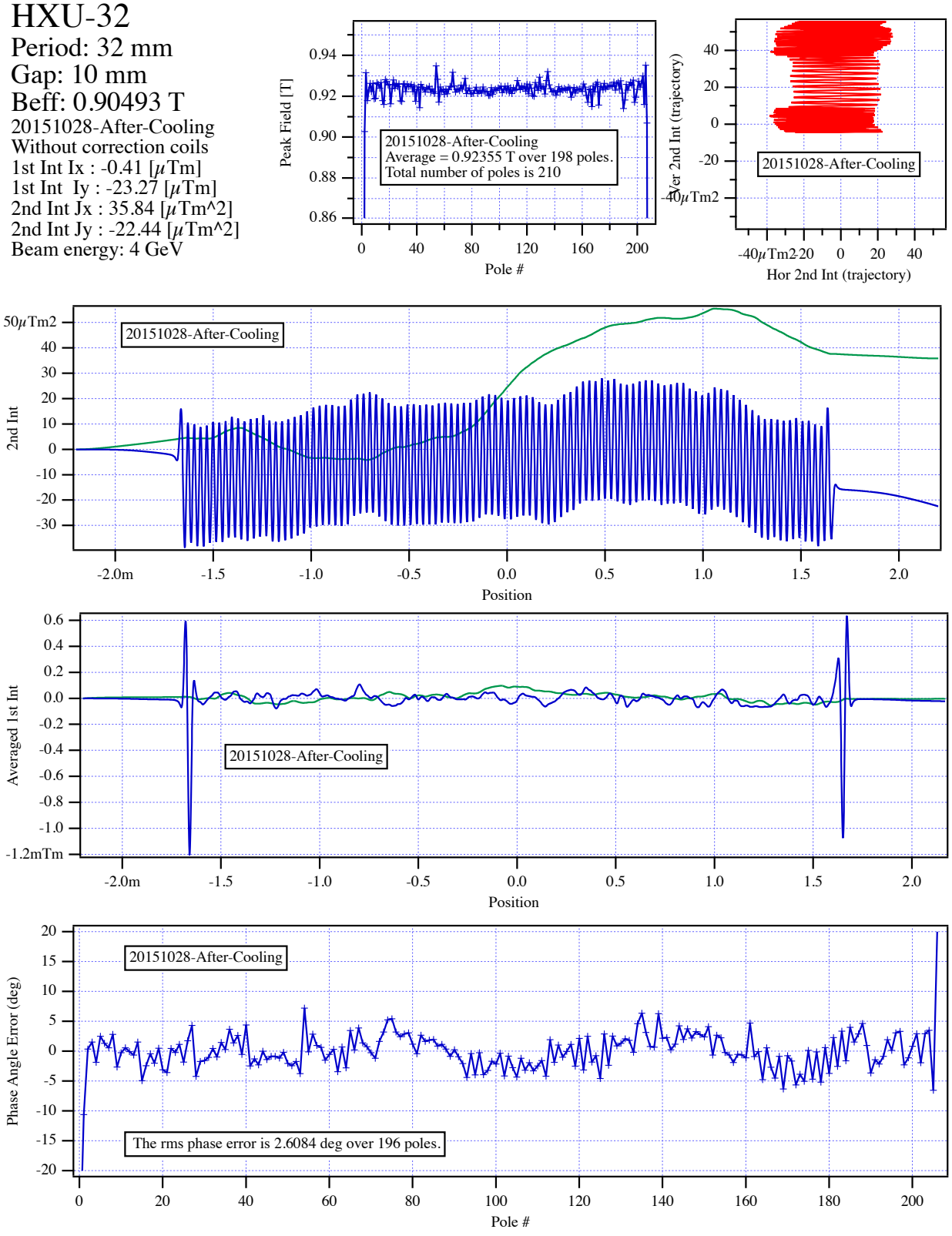

Figure 11: The measured fields, angles, trajectories and phase errors for the HXU-32 at 10 mm gap.

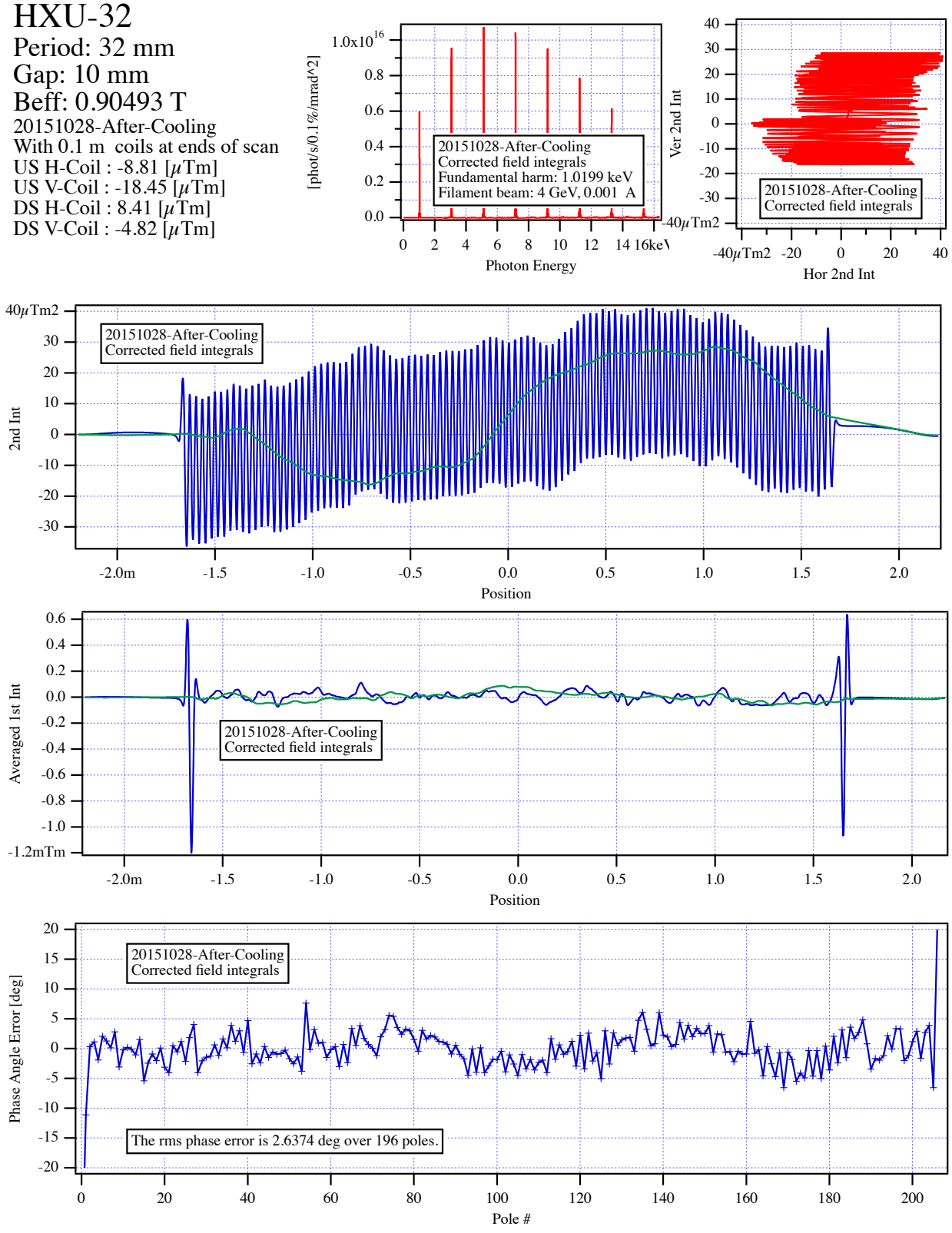

Figure 12: The measured fields, angles, trajectories and phase errors for the HXU-32 at 10 mm gap with the beam path corrected by virtual coils.

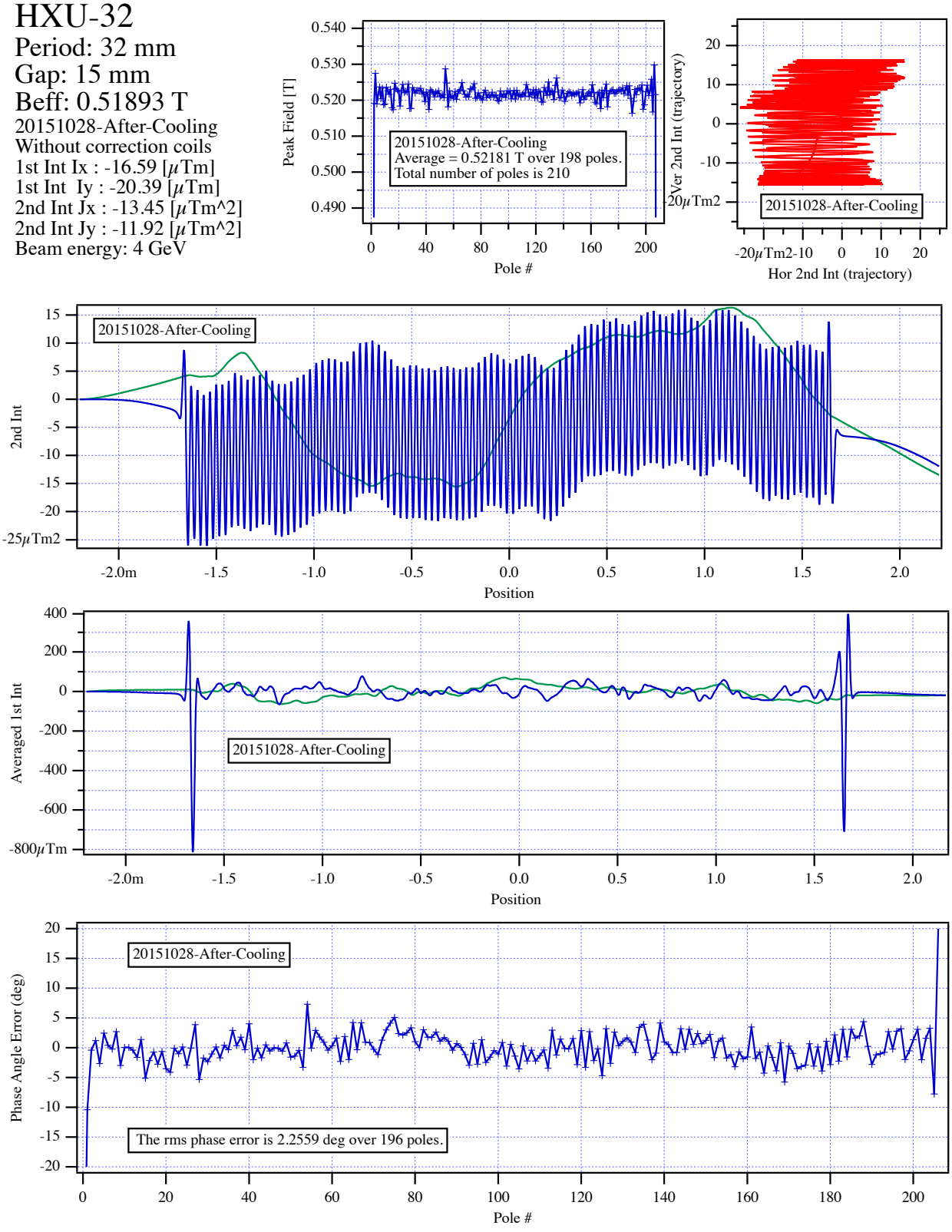

Figure 13: The measured fields, angles, trajectories and phase errors for the HXU-32 at 15 mm gap.

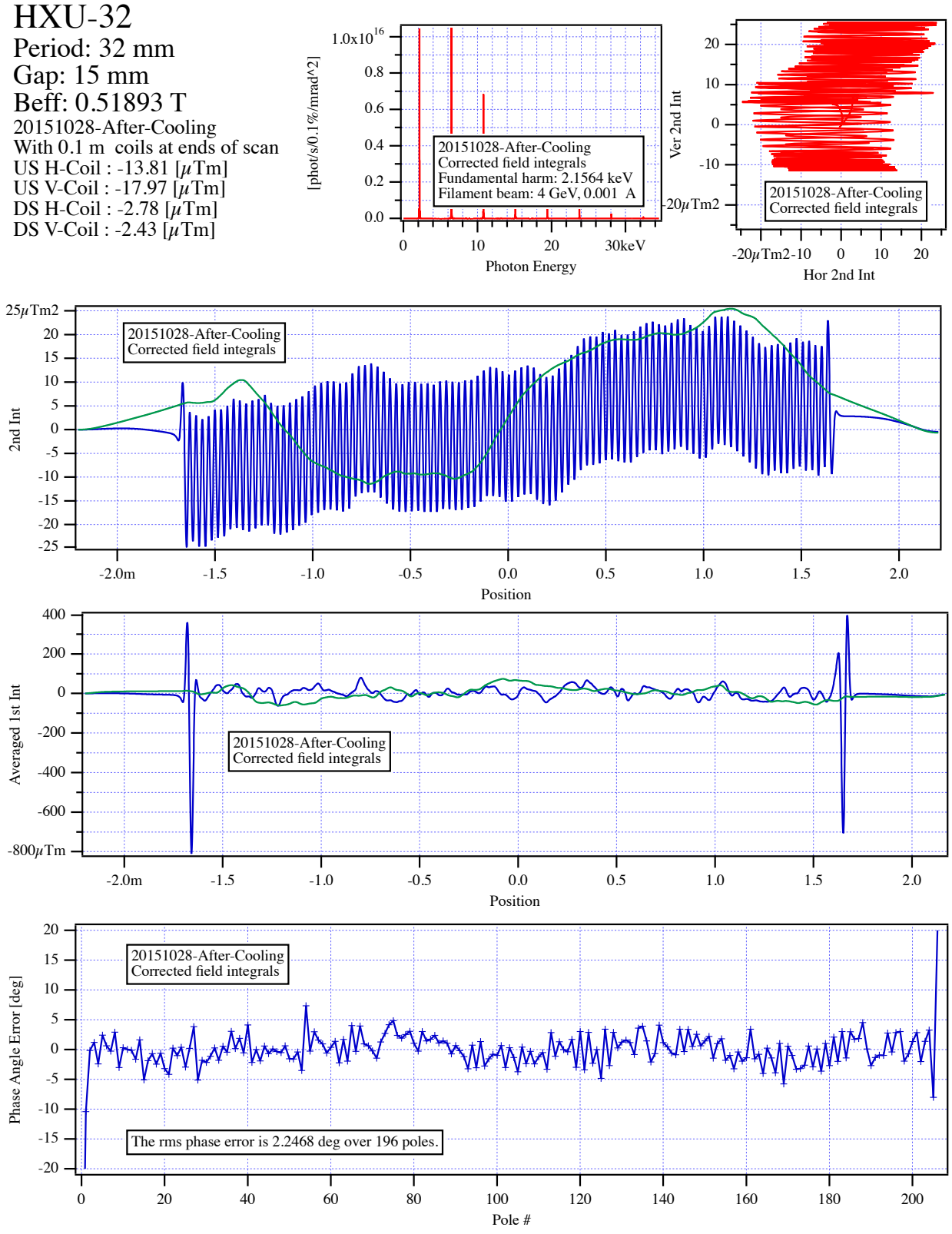

Figure 14: The measured fields, angles, trajectories and phase errors for the HXU-32 at 15 mm gap with the beam path corrected by virtual coils.

HXU-32
Period: 32 mm
Gap: 20 mm
Beff: 0.30989 T
20151028-After-Cooling
Without correction coils
1st Int Ix : -16.55 [μTm]
1st Int Iy : -20.42 [μTm]
2nd Int Jx : -17.17 [μTm^2]
2nd Int Jy : -4.73 [μTm^2]
Beam energy: 4 GeV

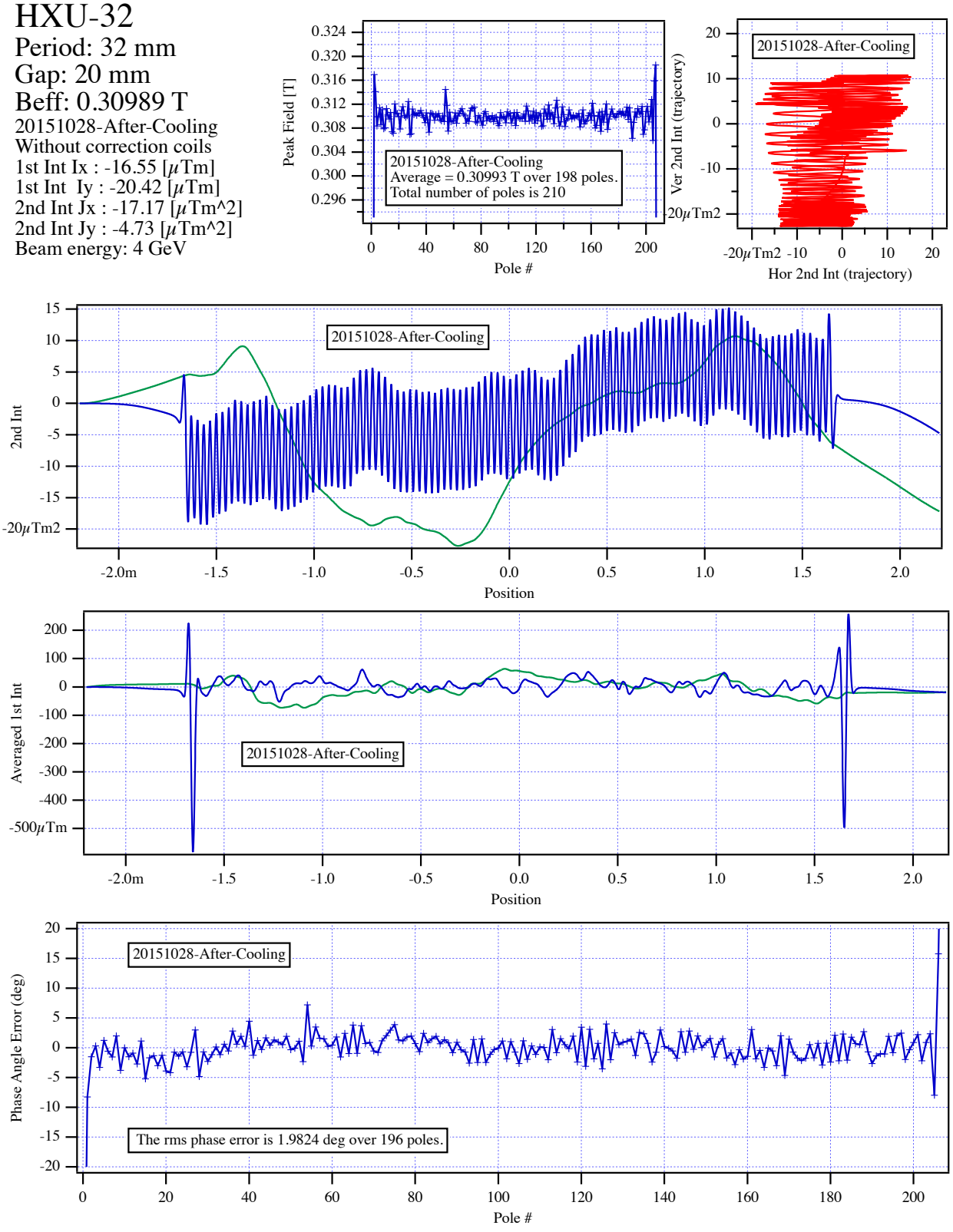

Figure 15: The measured fields, angles, trajectories and phase errors for the HXU-32 at 20 mm gap.

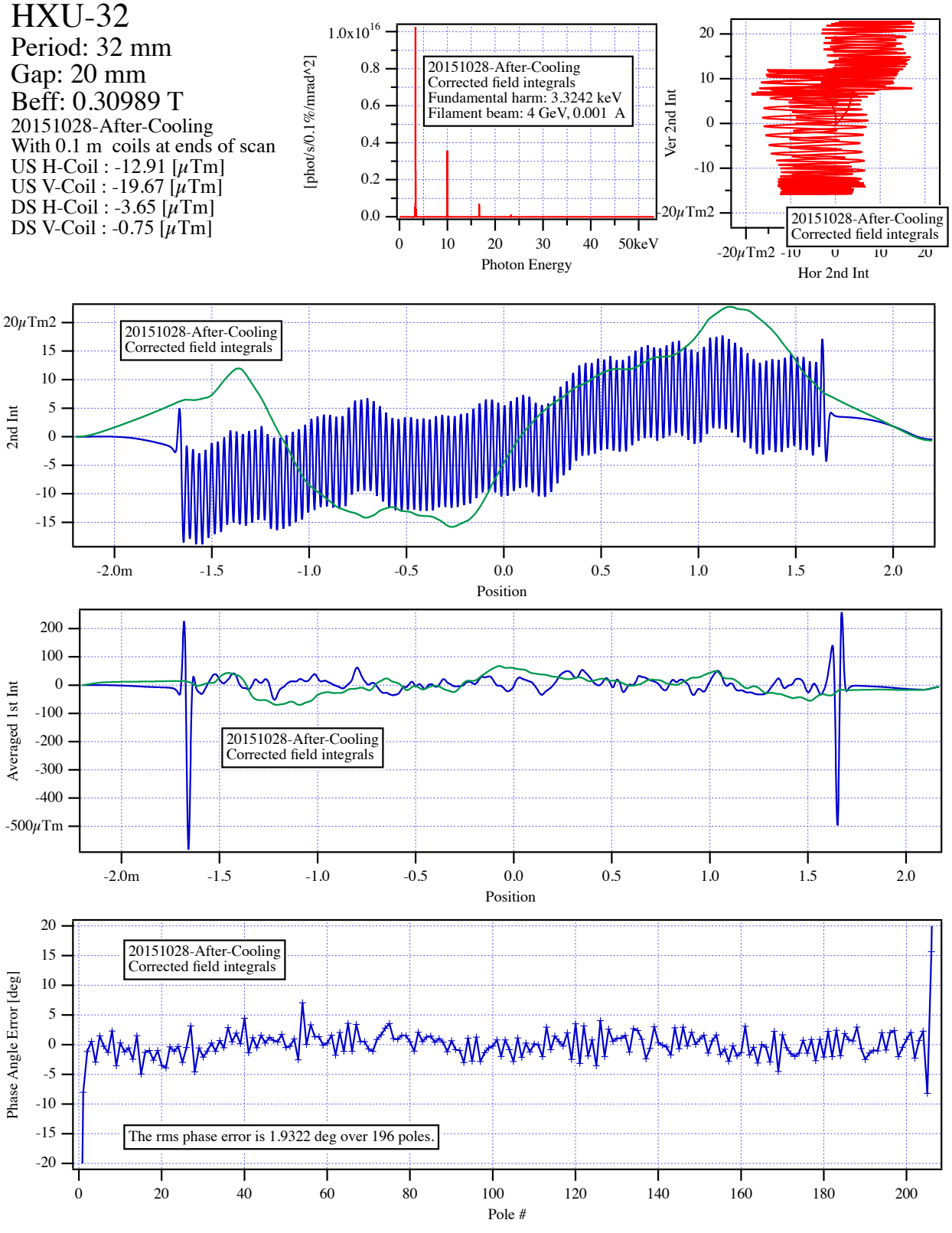

Figure 16: The measured fields, angles, trajectories and phase errors for the HXU-32 at 20 mm gap with the beam path corrected by virtual coils.

HXU-32
Period: 32 mm
Gap: 25 mm
Beff: 0.18769 T
20151028-After-Cooling
Without correction coils
1st Int Ix : -5.8 [μTm]
1st Int Iy : -22.58 [μTm]
2nd Int Jx : 10.45 [μTm^2]
2nd Int Jy : -3.33 [μTm^2]
Beam energy: 4 GeV

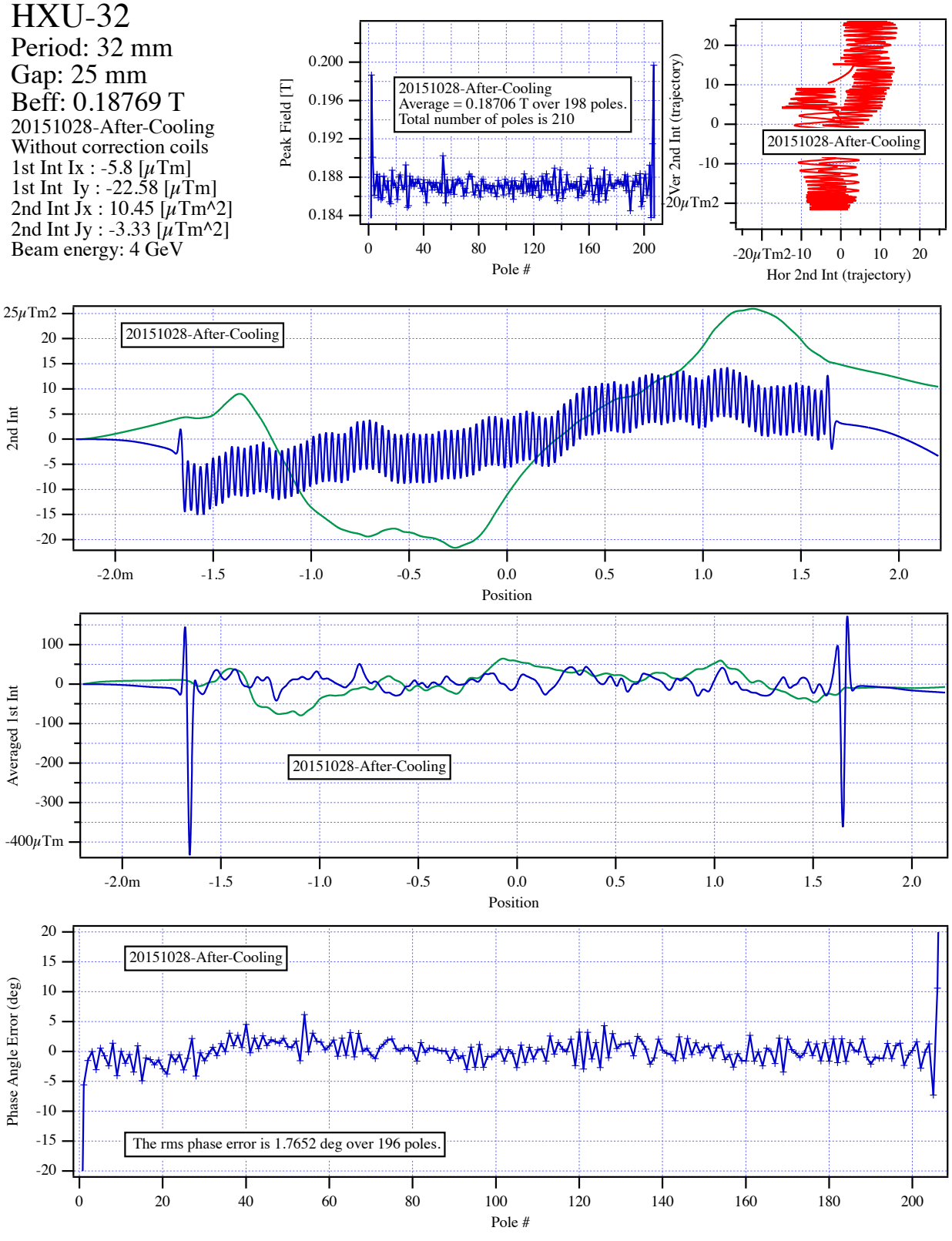

Figure 17: The measured fields, angles, trajectories and phase errors for the HXU-32 at 25 mm gap.

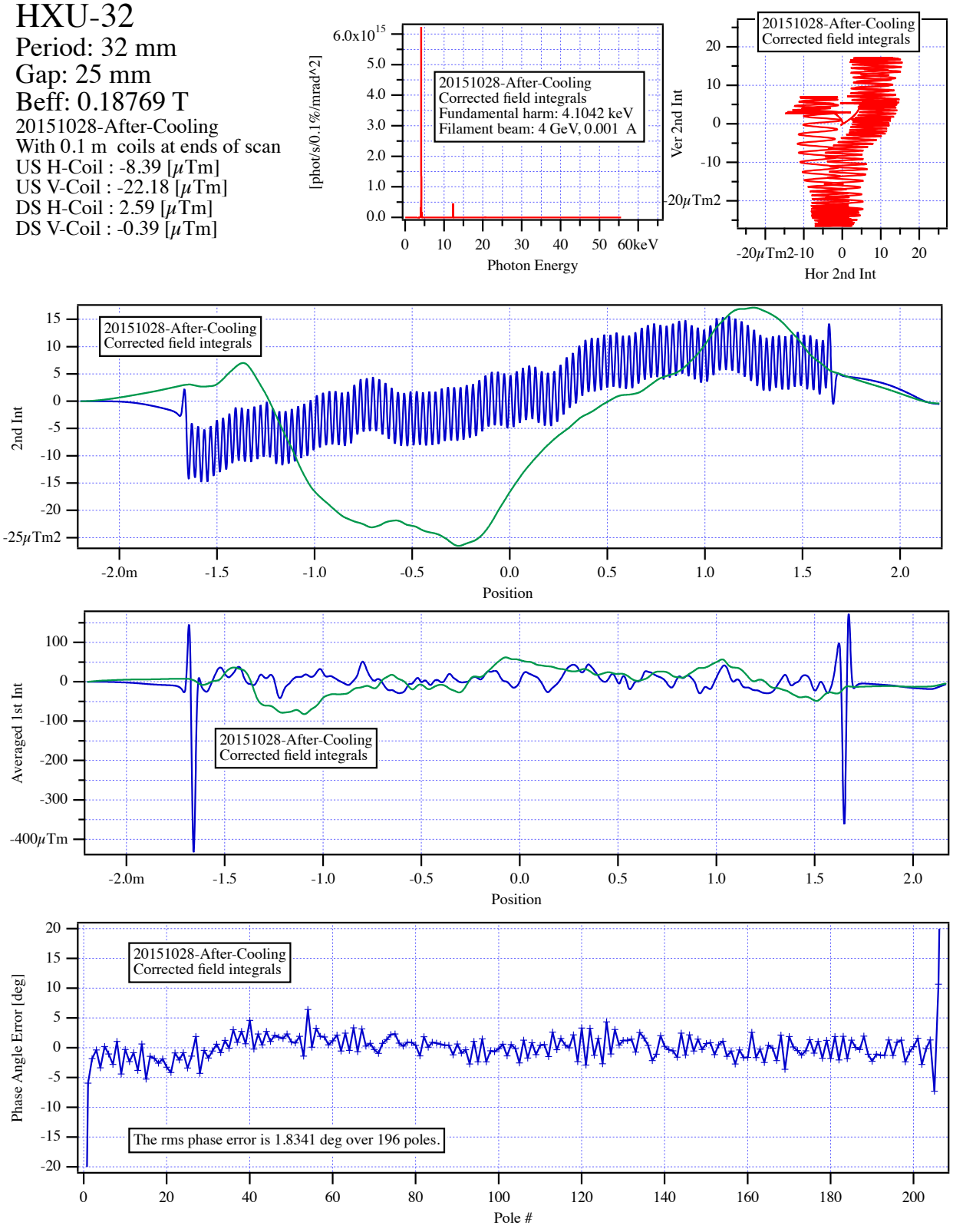

Figure 18: The measured fields, angles, trajectories and phase errors for the HXU-32 at 25 mm gap with the beam path corrected by virtual coils.

5.7 Gap 50, 100 and 180 mm

The measured vertical fields for the gaps 50, 100 and 180 mm are shown in Figure 19 and the corresponding horizontal fields are shown in Figure 20 .

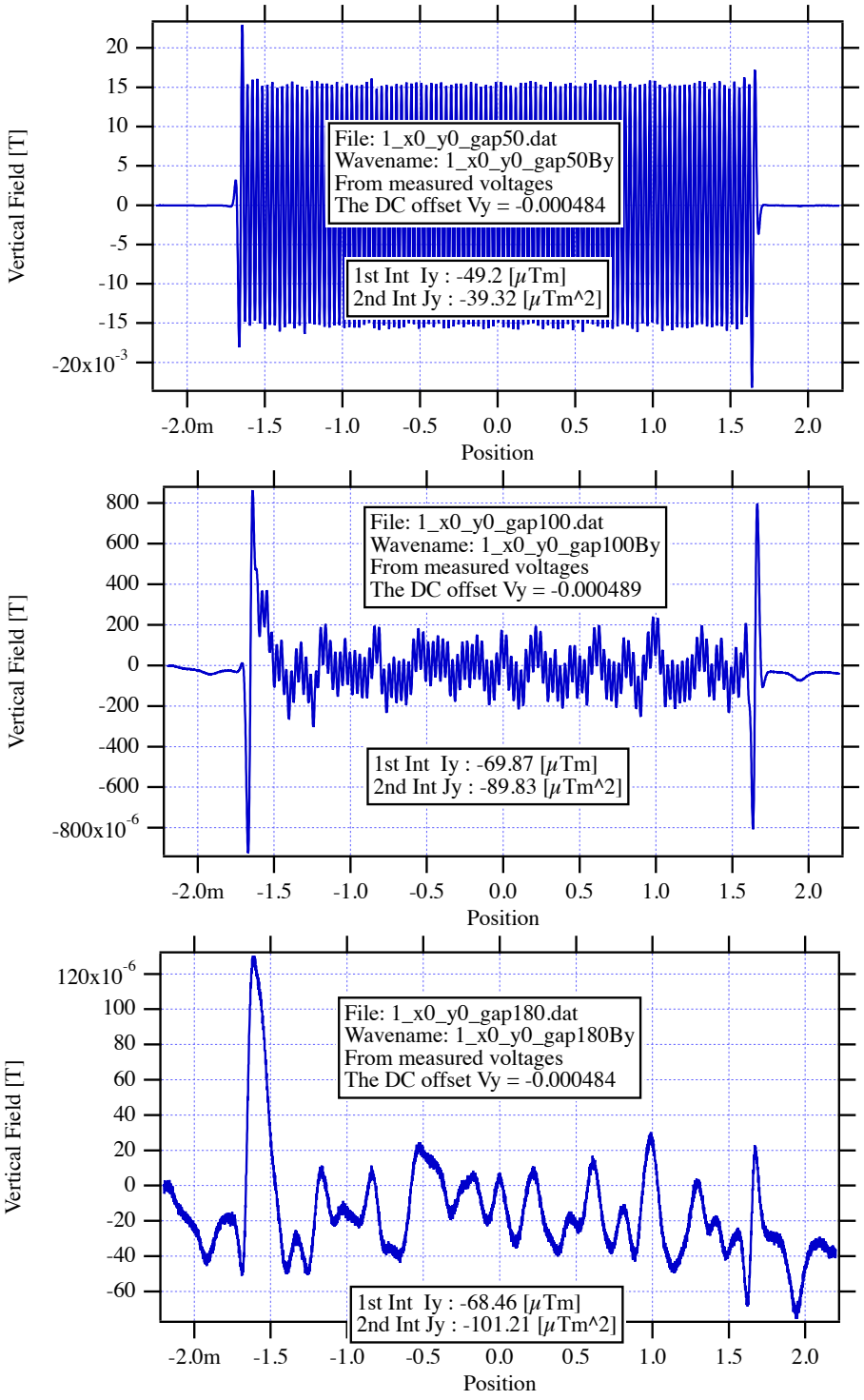

Figure 19: The measured vertical fields for the HXU-32 at the gaps 50, 100 and 180 mm.

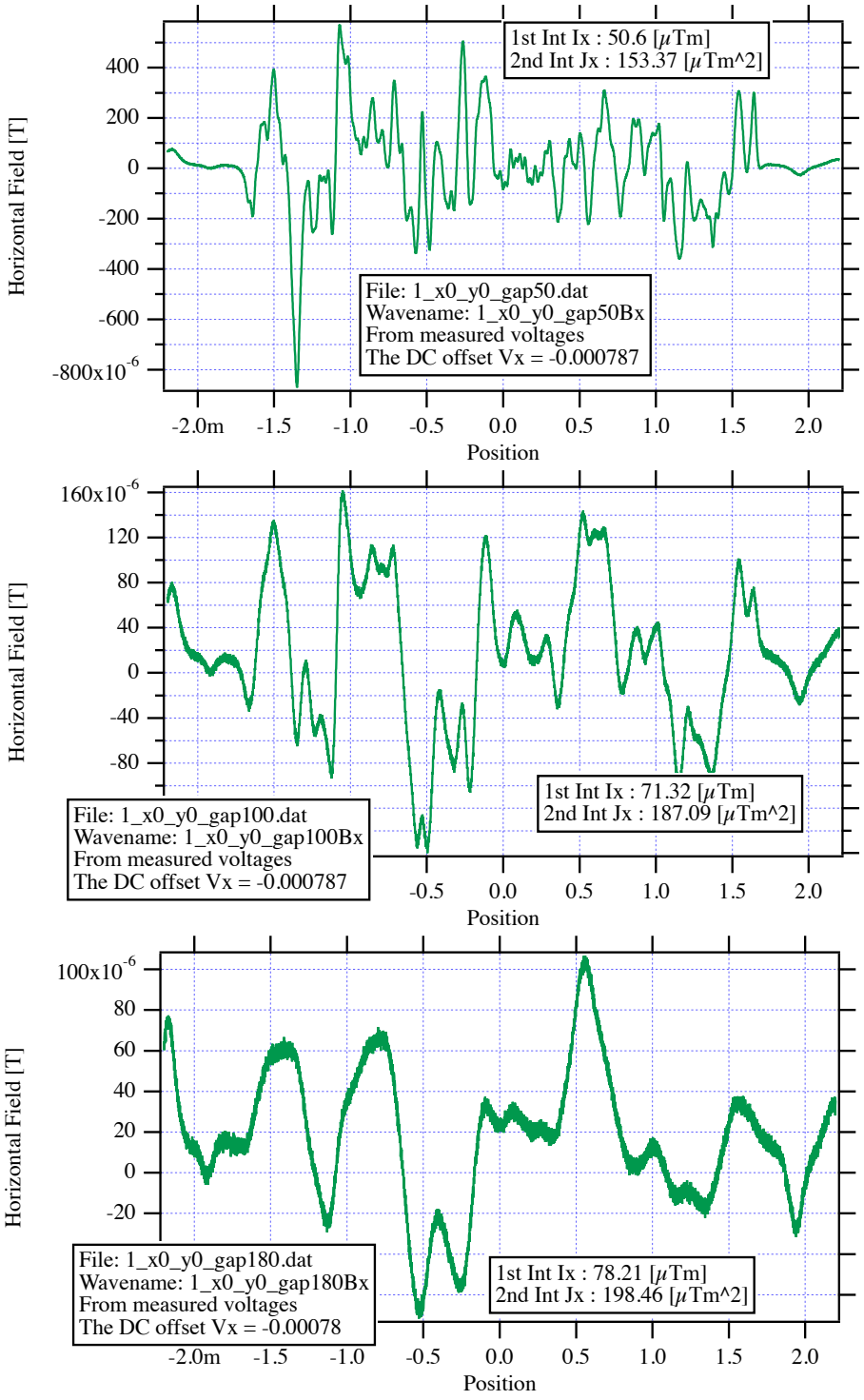

Figure 20: The measured horizontal fields for the HXU-32 at the gaps 50, 100 and 180 mm.

6 Repeatability of the effective field

The repeatability of the effective field has been measured by making 10 cycles over 8 gaps, giving in 80 measurements. The 8 gaps in the cycle ar 7.2, 8, 10, 15, 20, 15, 10, and 8 mm. The effective field has here, in the case of the repeatibilty measurements, been calculated using a fourier analysis of the measured magnetic fields.

Figure 21 shows the gaps during the repeatbility measurements. Figure 22 shows the measured effective field duing the repeatbility measurements. Figure 23 shows the measured deviation of the effective field duing the repeatbility measurements. Figure 24 shows the measured deviation of the effective field duing the repeatbility measurements as a function of the gap.

Table 3 shows data from the repeatability measurements.

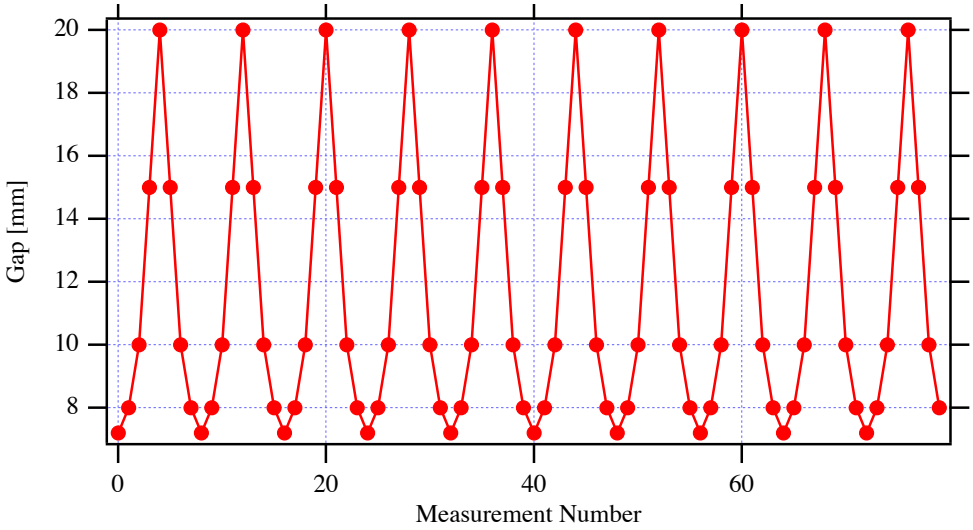

Figure 21: The gaps at the reapatability measurements of the effective field.

Table 3: Data from Beff repeatability measurements

Gap mm	Aver Beff T	RMS Dev G	RMS Dev $\times 10^{-4}$	Max ΔBeff/Beff $\times 10^{-4}$	Min ΔBeff/Beff $\times 10^{-4}$
7.2	1.2798	1.4783	1.1551	1.3066	-2.2664
8	1.1569	1.5267	1.3197	2.6311	-1.7998
10	0.9034	1.2242	1.3551	2.4357	-1.5586
15	0.51787	0.39591	0.7645	1.1168	-1.2162
20	0.30907	0.067761	0.21924	0.40624	-0.28899

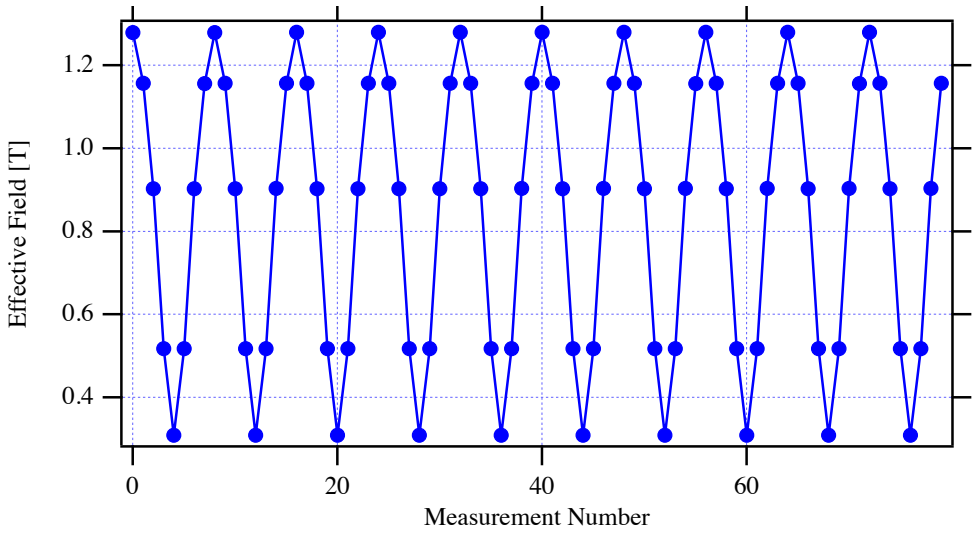

Figure 22: The measured effective field at the reapatability measurements.

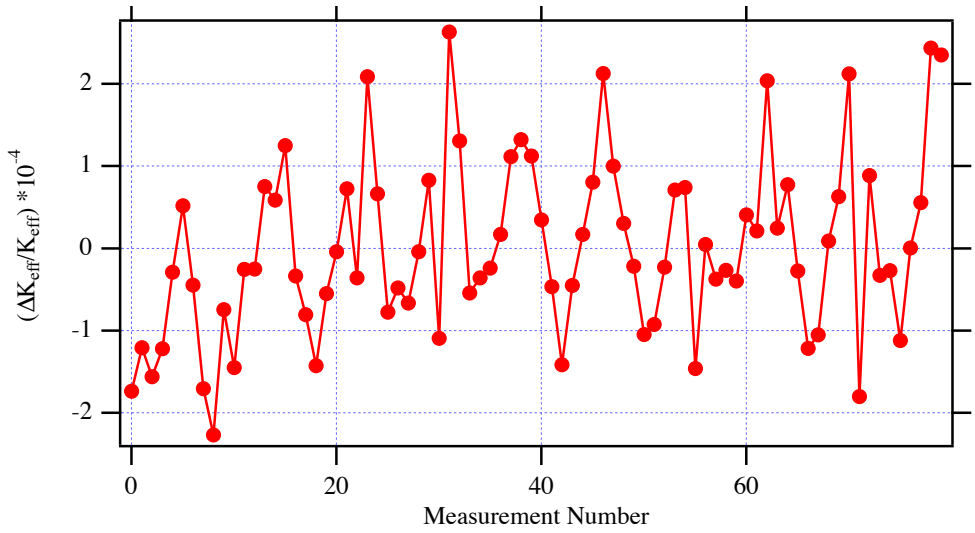

Figure 23: The measured deviation of the effective field at the reapatability measurements.

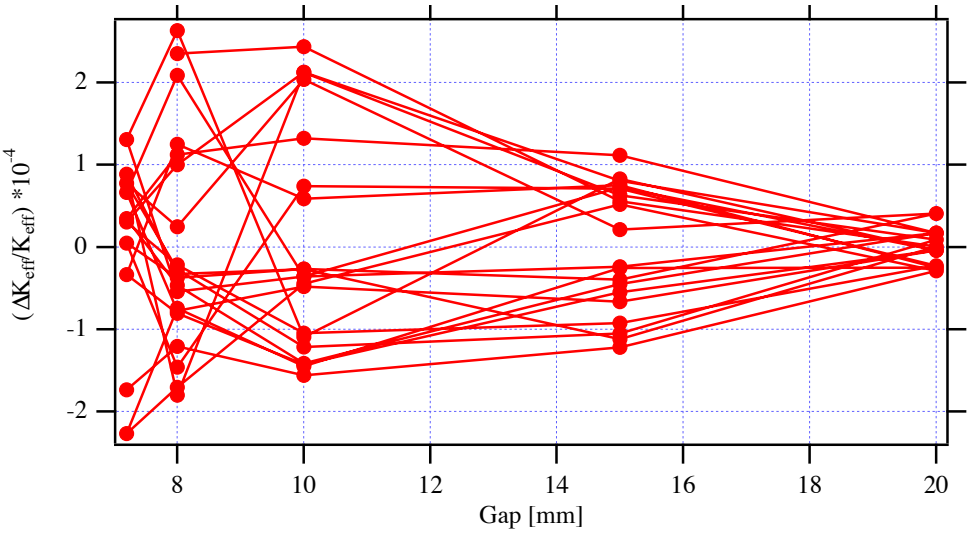

Figure 24: The measured deviation of the effective field at the reapatability measurements as a function of the gap.

7 Off-axis measurements

The field integrals and fields have been measured at distances ± 1 mm out from the undulator axis. The measurements lines are called P1-P5 as illustrated in Figure 25.

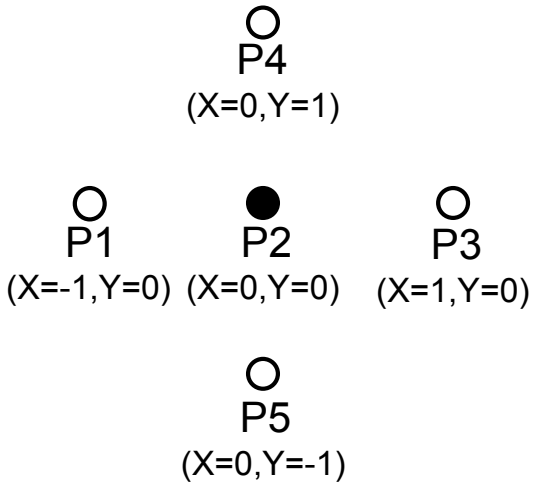

Figure 25: Off-axis points named P1-P5. X and Y are the horizontal and vertical positions in mm. The undulator axis is at X=Y=0. The scan is carried out in the Z-direction in a right handed XYZ coordinate system.

The effective fields, the RMS phase errors, and the first and second field integrals from the off-axis measurements are given in Table 4. The second field integrals along the scans, which gives the trajectory, are shown in Figures 26 to 30 . The phase errors along the scans are shown in Figures 31 to 35 .

Table 4: Data from off-axis measurements

Point	Gap mm	Beff T	Phase Error ° RMS	I1X μTm	I1Y μTm	I2X μTm^2	I2Y μTm^2
P1	7.2	1.2826	2.9643	1.1	-20.6	56.6	66.2
P2	7.2	1.2821	2.9868	-15.2	-22.6	-1.1	55.7
P3	7.2	1.2820	2.9000	-25.8	-20.2	-45.3	62.3
P4	7.2	1.3076	5.3180	-8.8	-40	11.8	31.8
P5	7.2	1.3068	4.5526	-12.5	-14.2	7.2	50.4
P1	8	1.1592	2.9453	5.2	-16.1	76.9	-11.5
P2	8	1.1591	2.8815	-2.7	-23	37.4	-29.6
P3	8	1.1590	2.8199	-10.9	-23.2	0.2	-28.6
P4	8	1.1821	5.0154	-0.4	-35.1	41.8	-40.2
P5	8	1.1814	4.5636	-6.4	-16.5	29.5	-37.1
P1	10	0.90503	2.6718	7.9	-18.7	71.6	-13.9
P2	10	0.90506	2.6688	1.0	-23.3	41.6	-25.5
P3	10	0.90501	2.5935	-6.4	-23.3	11.8	-21.6
P4	10	0.92301	4.4531	5.2	-33.5	51.8	-35.6
P5	10	0.92252	4.7675	-0.7	-18.2	35.6	-28.4
P1	15	0.51898	2.2977	-17.2	-22.3	-6.2	-18.4
P2	15	0.51900	2.3073	-14.3	-22.9	-9.6	-22
P3	15	0.51896	2.3085	-15.5	-20.9	-18.8	-14.7
P4	15	0.52924	3.1971	-14.5	-24.1	-8.3	-15.4
P5	15	0.52897	3.984	-13.2	-24.7	-2.1	-34.4
P1	20	0.30993	2.007	-18.7	-23.7	-10.8	-13.9
P2	20	0.30995	1.9758	-13.0	-21.3	-4.1	-8.6
P3	20	0.30989	1.9314	-15.7	-18.7	-18.1	-6.6
P4	20	0.31606	2.3396	-16.6	-20.9	-15.9	-0.8
P5	20	0.31589	2.7561	-14.5	-25.2	-7.5	-25

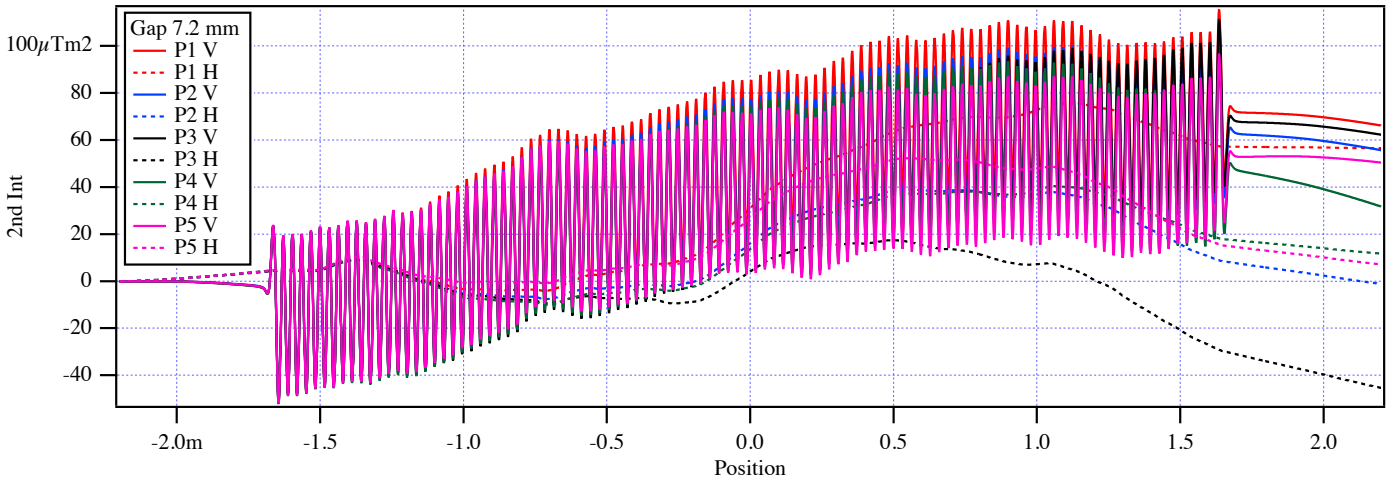

Figure 26: The second field integrals along the off-axis scans, which give the trajectories, at 7.2 mm gap.

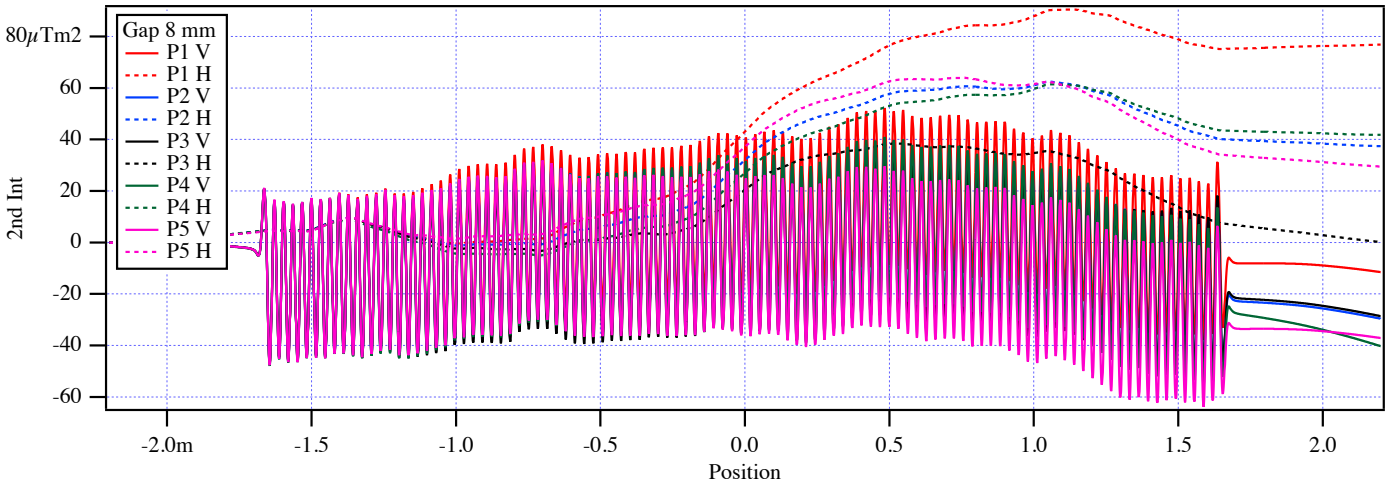

Figure 27: The second field integrals along the off-axis scans, which give the trajectories, at 8 mm gap.

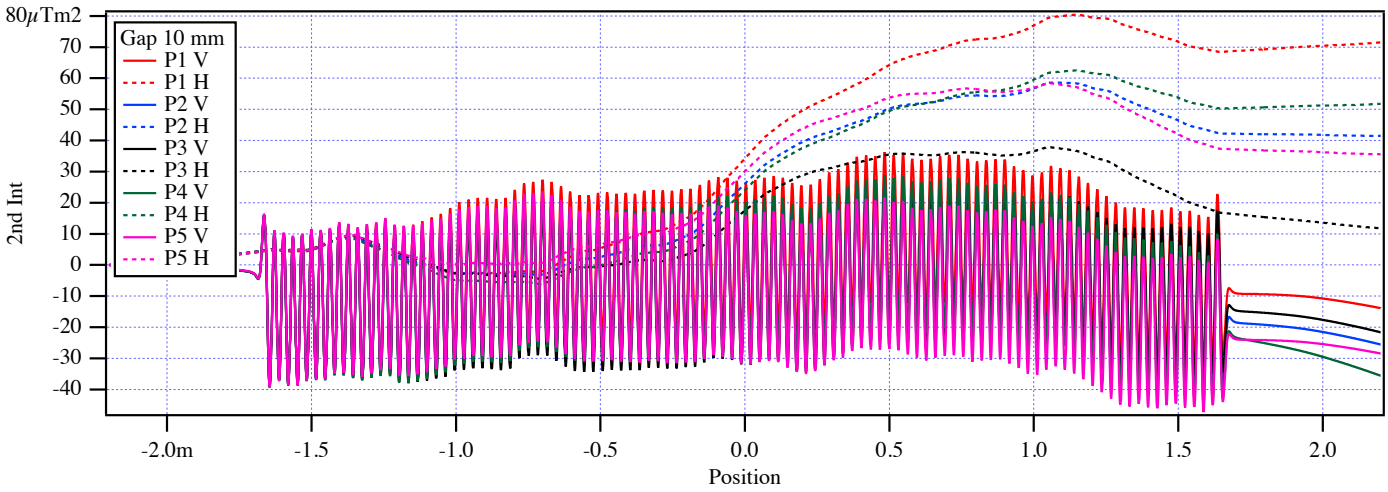

Figure 28: The second field integrals along the off-axis scans, which give the trajectories, at 10 mm gap.

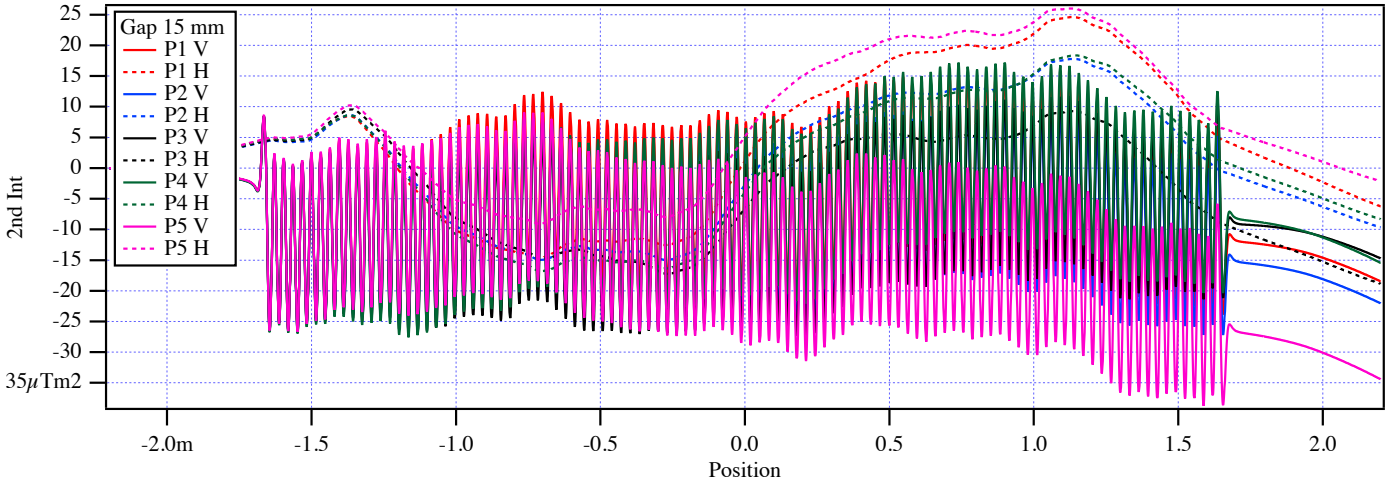

Figure 29: The second field integrals along the off-axis scans, which give the trajectories, at 15 mm gap.

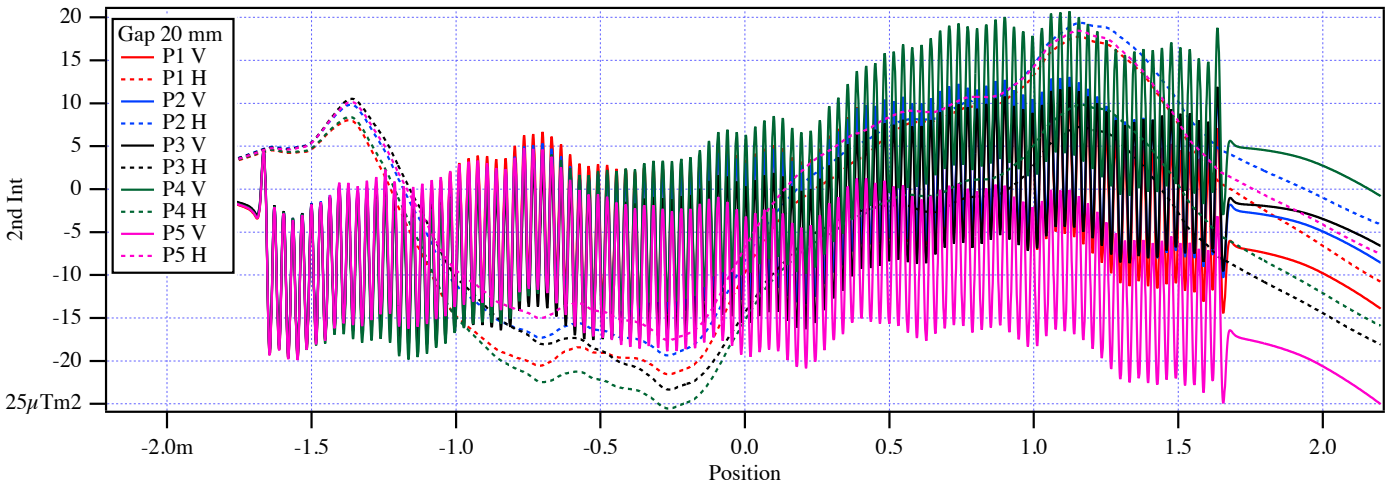

Figure 30: The second field integrals along the off-axis scans, which give the trajectories, at 20 mm gap.

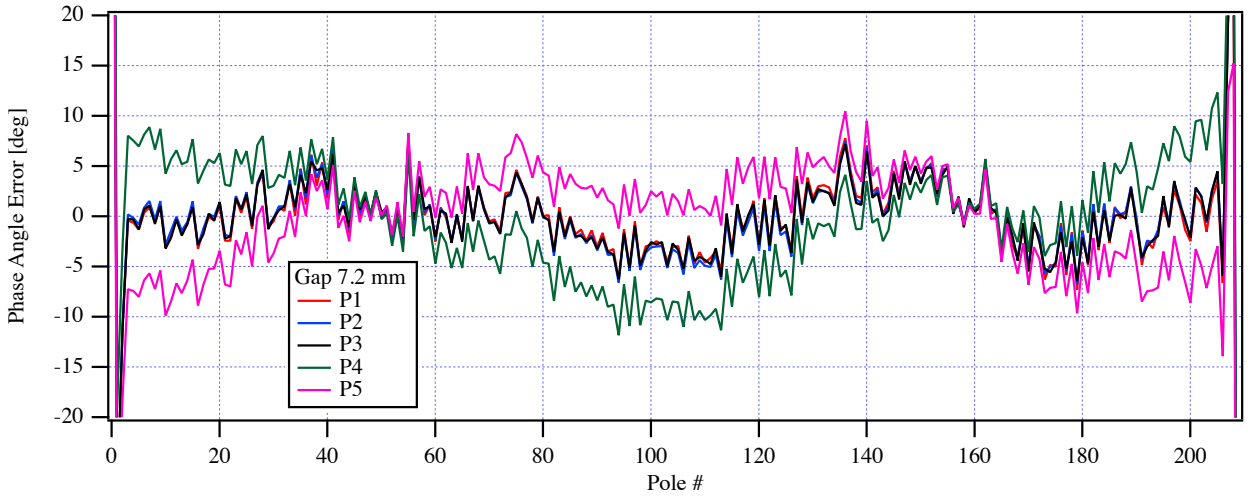

Figure 31: The sphase errors along the off-axis scans at 7.2 mm gap.

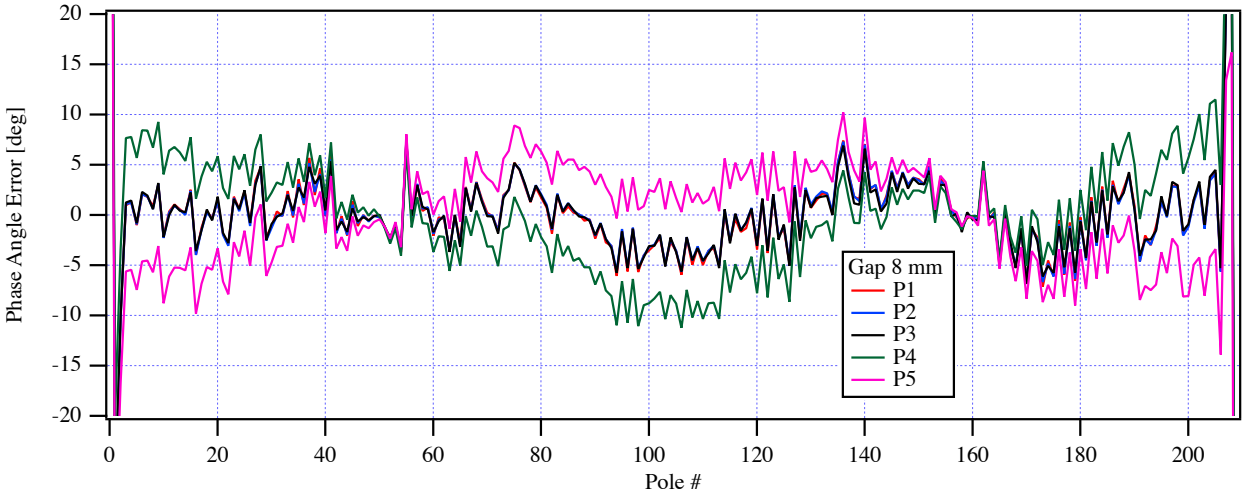

Figure 32: The sphase errors along the off-axis scans at 8 mm gap.

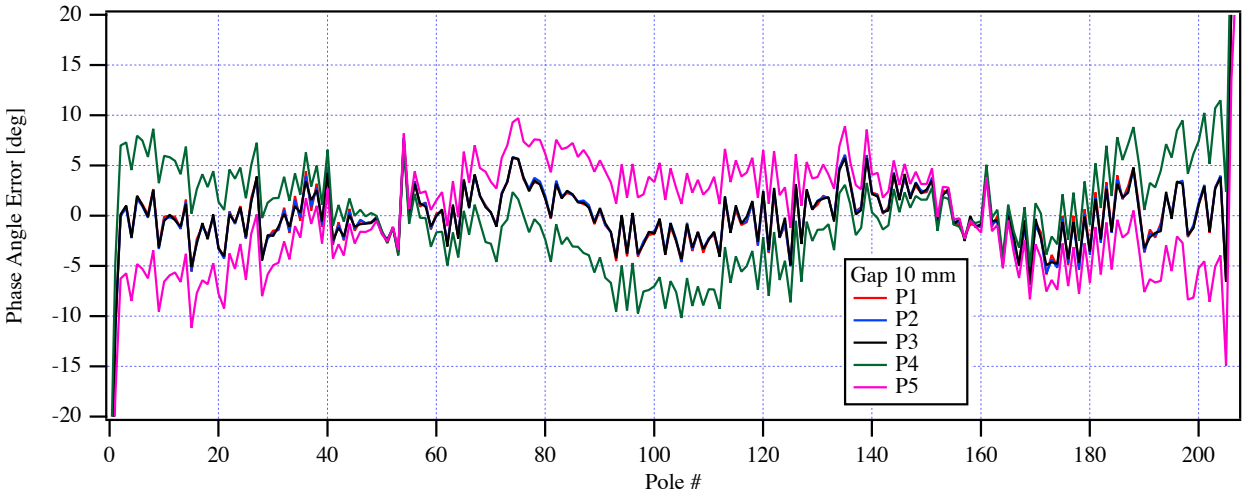

Figure 33: The sphase errors along the off-axis scans at 10 mm gap.

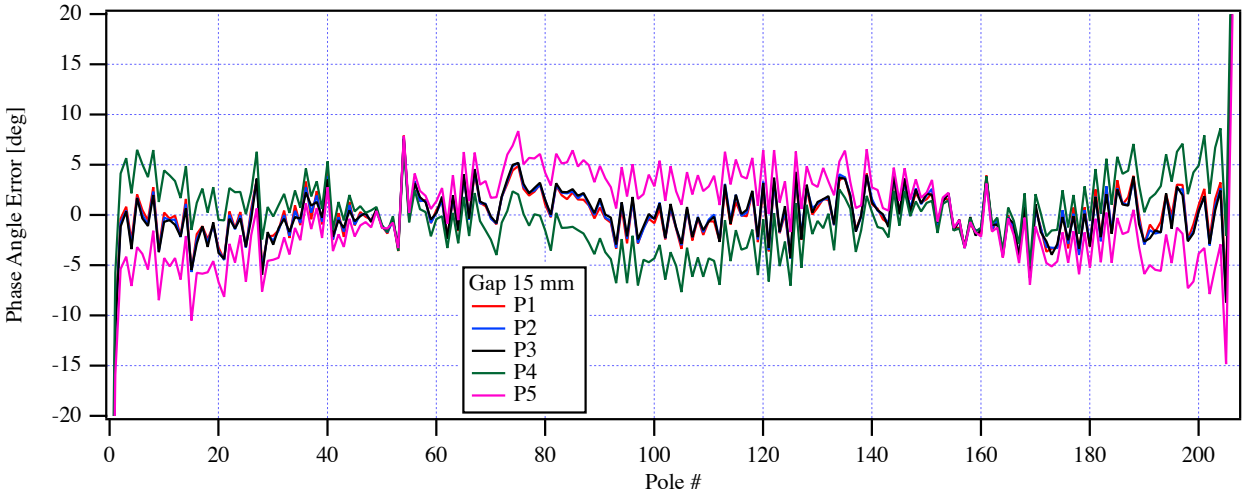

Figure 34: The sphase errors along the off-axis scans at 15 mm gap.

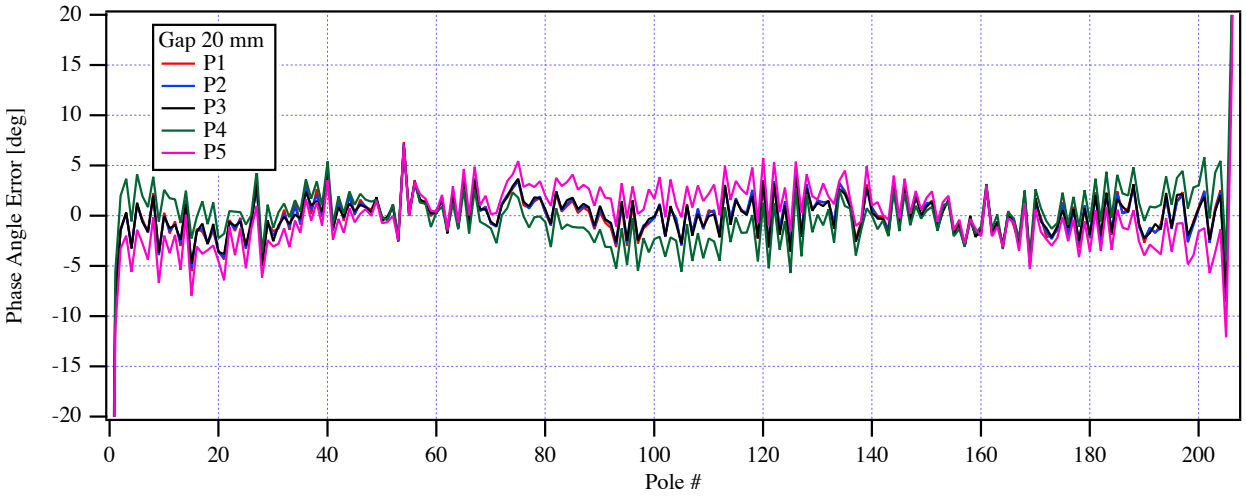

Figure 35: The sphase errors along the off-axis scans at 20 mm gap.

8 Measurement of the uniformity of the effective field

The effective magnetic field has been measured at distances ± 1 mm out from the undulator axis at two different gaps. The measurement lines are called T1-T9 as illustrated in Figure 36. The effective field has here, in the case of the unformity measurements, been calculated using a fourier analysis of the measured magnetic fields.

The effective field B_{eff} on the undulator axis is given by

$$B_{eff} = \sqrt{\sum_{n=1}^{\infty} \frac{1}{n^2} B_n^2} \tag{1}$$

where B_n is the strength of the harmonic with multiple n of the basic undulator periodicity. The effective fields and the fourier harmonics from the uniformity measurements are given in Table 5. The measured data shown in Table 5 has been used to plot the variation of the effective field over the central parts of the aperture as shownin Figure 37.

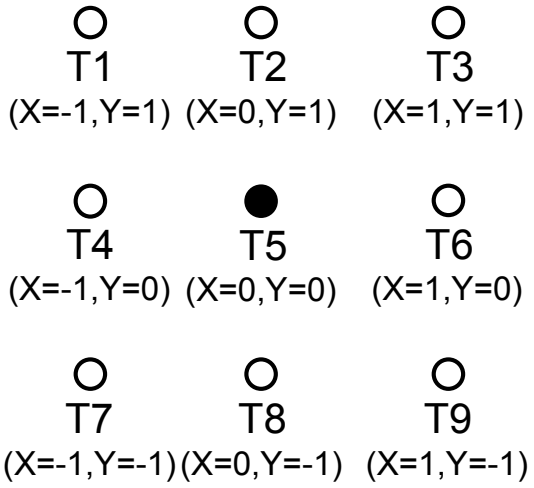

Figure 36: Off-axis points named T1-T9. X and Y are the horizontal and vertical positions in mm. The undulator axis is at $X = Y = 0$. The scan is carried out in the Z-direction in a right handed XYZ coordinate system.

The horizontal sextupole term of the effective field depending on the horizontal position X, $\left|\frac{1}{2}(1/B_{eff})\partial^2 B_{eff}/\partial X^2)\right|$, is 6.35e-05 mm^{-2} at the gap 20 mm and 1.24e-05 mm^{-2} at the gap 7.2 mm.

Table 5: Data from measurements of the uniformity of the effective field

Point	Gap mm	B_{eff} T	B_1 T	B_3 mT	B_5 mT
T 1	20	0.31514	0.31514	1.0316	0.035054
T 2	20	0.31517	0.31517	1.0312	0.034650
T 3	20	0.31513	0.31513	1.0313	0.035161
T 4	20	0.30904	0.30904	0.88314	0.024380
T 5	20	0.30907	0.30907	0.88275	0.024483
T 6	20	0.30903	0.30903	0.88283	0.024167
T 7	20	0.31500	0.31500	1.0293	0.034696
T 8	20	0.31503	0.31503	1.0282	0.034618
T 9	20	0.31498	0.31498	1.0281	0.034786
T 1	7.2	1.3053	1.3051	79.775	12.129
T 2	7.2	1.3049	1.3046	79.703	12.114
T 3	7.2	1.3048	1.3045	79.704	12.120
T 4	7.2	1.2797	1.2795	67.744	8.0925
T 5	7.2	1.2796	1.2794	67.723	8.0928
T 6	7.2	1.2795	1.2793	67.703	8.0907
T 7	7.2	1.3043	1.3040	79.386	12.059
T 8	7.2	1.3042	1.3039	79.355	12.055
T 9	7.2	1.3040	1.3037	79.315	12.051

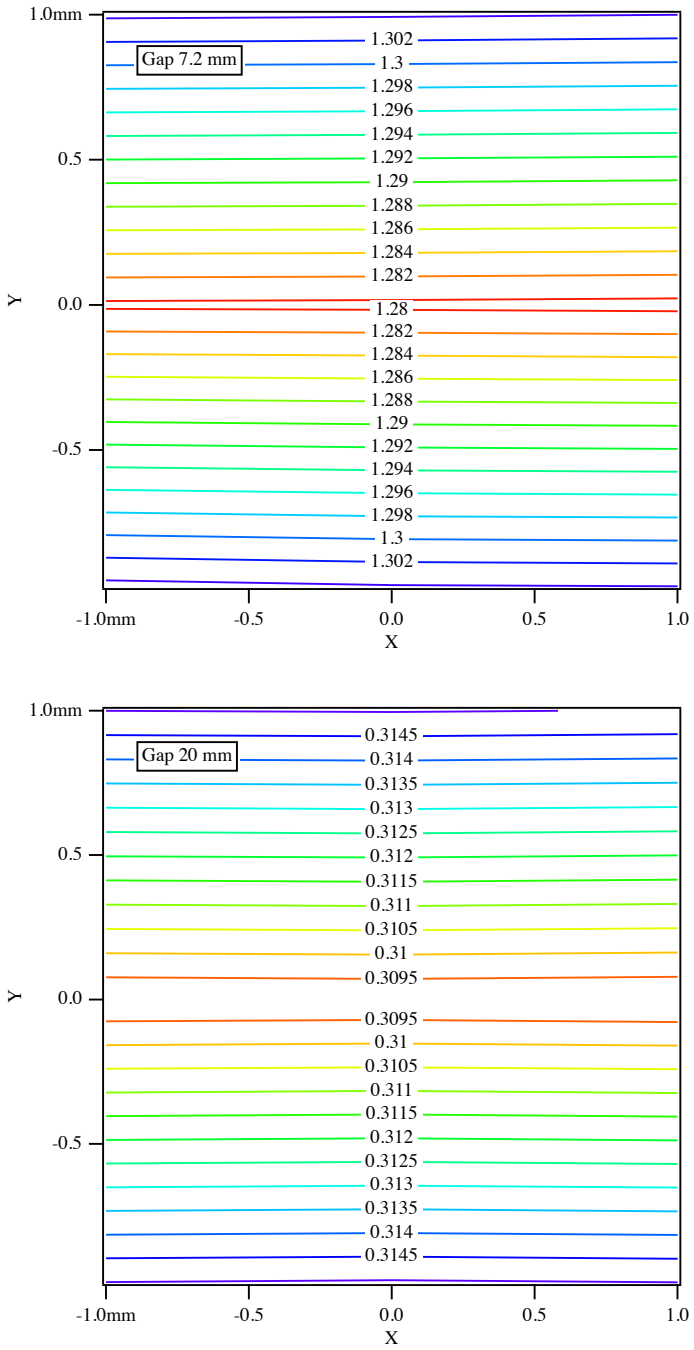

Figure 37: The variation of the effective field over the central parts of the undulator aperture at two different gaps. The data used for the plots are given in Table 5.